There Is Something In The Water

Fritz van Deventer
Thesis Report GIRS-2012-25
October, 2012

WAGENINGEN UNIVERSITY
WAGENINGEN UR

Water Insight

There is Something in the Water

Using Spectrometry and a 2D CCD Camera as an Integrated Device to Inquire After Water Quality Paramters

Author:
Fritz van Deventer

Supervisors:
Dr.Ir. J.G.P.W. Clevers
Dr. M.L. Laanen
A. Poortinga, MSc

A thesis submitted in partial fulfilment of the degree of Master of Science at Wageningen University and Research Centre, The Netherlands.

October, 2012
Wageningen, The Netherlands

Abstract

The assessment of water quality parameters, such as suspendid sediments and chlorophyll-a, through remotely sensed image using different hyperspectral sensors is common. However most of this data has a medium to low spatial and low spectral resolution. The WICAM provides high spatial and high spectral resolution by combining spectrometers and a spectral camera in its design. This research was carried out to investigate how the two types of measurements can be integrated into one water quality product. This was achieved by filtering the data to exempt wrong solar angles, and other sources of error from the dataset. The dataset was preprocessed and stored in a database from which most of the postprocessing could be performed. The camera pixels were related to the spectrometry radiance values, after which reflectances could be calculated. These reflectances serve as input for the water quality models available in literature. The results show that both the measurement types could be integrated quite well for the angles in which the spectrometer was measuring. The main source of variability is light, which manifested itself in different ways. For the angles further away from the device the results become less reliable. Other sources of distortion come from surface roughness, or waves. For further research in situ measurements validating the results of the WICAM would be imperative.

Acknowledgements

Contents

List of Figures

List of Tables

Chapter 1

Introduction

> "[...] Water is water! And east is
> east and west is west and if you
> take cranberries and stew them
> like applesauce they taste much
> more like prunes than rhubarb
> does. Now, uh... now you tell me
> what you know."
>
> Groucho Marx

Water is the most valuable resource on earth, as it forms the basis of all life that exists. Unfortunately, this resource has come under constant stress from a quantitative as well as a qualititative point of view, due to population growth and ever increasing economic activities (Govender et al., 2007; Vorosmarty et al., 2000). Therefore, monitoring the water quality has become an essential tool to assess and sustain this valuable resource. Traditional methods of assessing water samples are rather tedious and costly, considering the vast areas covered with water (Kirk, 1994). Therefore, optical devices have become commonly used tools to evaluate the water quality in a range of different spatial and temporal resolutions (IOCCG, 2000). The calculations on e.g. hyperspectral sensors can link water quality parameters directly with dissolved concentrations (Hakvoort et al., 2002). Important water quality parameters, total suspended matter (TSM), chlorophyll-a (CHL) and coloured disolved organic matter (CDOM), can be derived with high spatial, temporal and spectral resolution. Satellites or aerial images have thus become a very data rich source to acquire information on water quality of large water bodies, but still have limitations in their spectral and temporal resolution, not to mention their dependence on clear skies. Spectrometers on the other hand, are capable of assessing the water quality at a point scale with a very high spectral and temporal resolution. A combination of these tools would be ideal to assess water quality in great detail.

The WICAM (Water Insight Camera) is a device that combines spectrally dense point measurements with spatially explicit information. The WICAM is

in fact a combination of three spectrometers mounted on a camera equipped
with a revolving rotary filter in front of a 2D CCD sensor. Mounted on e.g.
the top of a building, the camera is able to acquire spatially explicit images
over different spectral bands, whereas the spectrometers obtain information
on the upwelling and downwelling radiance in a given direction, as well as
the downwelling irradiance. This combination sounds ideal, as it combines
spatial with spectral dense information. However, scientifically it is not clear
how these different types of measurements relate to each other, as images of
waters are complex to analyze due to the properties of water that cause re-
fraction, absorption and scattering of light in and on the water column (Kirk,
1994). Moreover, in shallow and coastal waters the soil surface below and sus-
pended sediments further alter the reflection signal to the sensor. Waves fur-
ther exacerbate some of the other complexities (sunglint, reflection) (IOCCG,
2000). The time interval between the measurements is also likely to have a
pronounced effect due to the change in surface roughness and therefore con-
ditions of the light interacting with the water surface (Cox and Munk, 1954;
Mobley, 1999).

This report is the result of a Master thesis research in which the WICAM
was investigated to find out how the WICAM is performing. The report starts
with an outline of theories and context for the field of water remote sensing.
The Context & Background chapter also eplains how the two devices that are
built into the WICAM work and what kind of output they give. After that
the problems and research questions are stated. The methodology chapter
explains how and what has been done to get results to the research questions.
The results are then portrayed and discussed after which the conclusions that
can be drawn and the recommendations that can be made from the research
are explained.

Chapter 2

Context & Background

Sometimes it's not enough to
know what things mean,
sometimes you have to know
what things don't mean.

———————————————————————

Bob Dylan

2.1 Water Remote Sensing

Remote sensing (RS) is a technique to detect radation emitted or reflected by
an object. Two different types of RS can be distinguished, namely active and
passive remote sensing. Active remote sensing uses an active lightsource, con-
trary to passive RS, where only the natural radiation or reflection of an object
is detected (Richards and Jia, 2006). In water remote sensing, passive remote
sensing is the commonly used method. This means that the method is de-
pendent on sunlight and subject to all kinds of interference and absorption
features of water. The signal to noise ratio is significantly lower than in other
fields of application such as soil or vegetation, as water bodies are dark and
therefore reflect less. When there is a high amount of reflection of sun on the
surface of the water, the signal that can be received at the sensor is mostly
from the sun reflecting on the surface (Gons, 1999). It is therefore imperative
to understand the preferred procedures of measuring the light field in a water
body, that can be used to arrive at water quality products. In order to under-
stand the theory behind water remote sensing, we have to follow the pathway
of light into the water.

A Photon Reaching Water

A travelling photon from the sun can be scattered or absorbed by particles
it encounters (as seen in Figure 2.1), it is scattered until all of the light is ab-
sorbed. In the atmosphere this scattering can be due to aerosols, water vapour,
dust particles and so forth. Whereas in the water there are 4 major components

3

that light absorption in the water can be ascribed to: water itself, dissolved yellow pigments or Coloured Dissolved Organic Matter (CDOM), phytoplankton or algae and cyanobacteria (commonly referred to with their main component Chlorophyll-a (CHL)) and inanimate suspended material or total suspended matter (TSM) (e.g. detritus, soil particles etc.)(Kirk, 1994). All of these features have their own distinctive absorption and scattering features and different species and growth stages again have different spectral reflectance curves (Arrigo et al., 1998; Bricaud et al., 1988; Kiefer et al., 1979; Kirkpatrick et al., 2000). In Figure 2.1 a number of these pathways of photons are described. Unfortu-
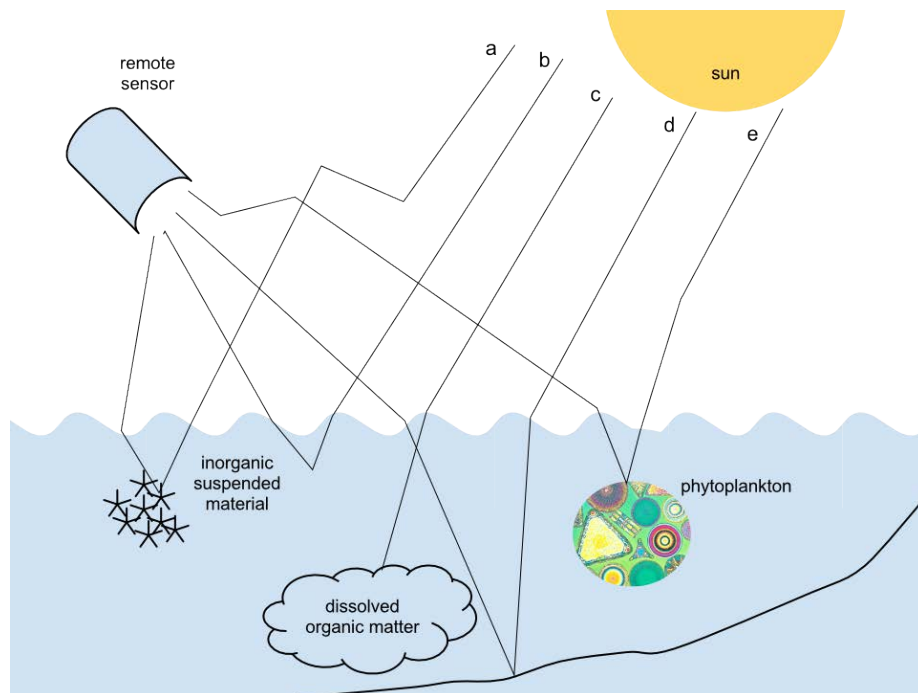
Figure 2.1: Different pathways of sunlight travelling through water to the sensor. Light is scattered by the particles it encounters until it is absorbed. Adapted from (IOCCG, 2000).

nately the situation in Figure 2.1 is oversimplified and overestimating the light reaching the sensor through the water. According to Morel (1980) over 80% of the light reaching the sensor can have an atmospheric source and does not originate from the water. In fact most information about the light field in water can be obtained from below the water surface. However, the measurements above water can cover larger areas in a short amount of time than the underwater measurements of the light field (Kirk, 1994).

The pathway of light is interesting enough in itself, but becomes of importance because of the application. According to the IOCCG (2000): "the goal of remote-sensing of ocean colour is to derive quantitative information on the types of substances present in the water and on their concentrations, from variations in the spectral form and magnitude of the ocean-colour signal." To

arrive at this information a step must be made from the measured radiance to the actual elements and their concentration.

The water quality parameters are derived from what are called apparent optical properties (AOP). Most importantly these are: ocean colour, reflectance R and the diffuse attenuation coefficient for upwelling irradiance K_d (IOCCG, 2000). A few properties important to measuring the light field from above the water surface will be explained in further detail in the following section. These AOPs are dependent on the element's inherent optical properties (IOP) and the angle of light (Preisendorfer, 1961, 1976). The IOPs determine how much and which part of the light is absorbed and which is scattered and do not change under different light conditions. These specific absorption and scattering properties can be related to the 3 major components other than water (CDOM, CHL and TSM) and their concentrations that account for the absorption in waters. The IOPs are derived from the AOPs, which can be calculated using the measured reflectance of a water body. Over the last few decades water remote sensing has come up with best practices and standards of measuring the light field above the water surface.

Measuring Light Above The Water Surface

Measuring the light above the water surface is most easily executed by measuring the sky downwelling radiance (L_{sky}), the sky downwelling irradiance (E_{sky}) and the water upwelling radiance (L_{water}) (Laanen, 2007). The irradiance measurements are done using cosine collectors. For practical purposes Gons (1999) suggests that the optimal measuring angle for the radiance measurements is at nadir angle $42°$. Although radiance measurements L_{water} are nearly constant at $0 - 30°$ nadir, they often introduce measuring station shadow (Laanen, 2007). Furthermore sky reflection of the air on the water surface is lower when measuring at $< 50°$ nadir, $42°$ is therefore considered optimal (Gons, 1999; Laanen, 2007). To correct for the radiance that is reflected on the water surface of (sky) downwelling radiance L_{sky} at the same angle a measurement is used. From these measurements a number things can be derived. For an overview of all the symbols used in the equations in this section see Table 2.1

In water remote sensing a convenient measure according to (Dekker, 1993) for the reflectance of the underwater light field is the subsurface irradiance reflectance at a minimal distance under the water surface $R(0^-)$ defined as the ratio between the upwelling and the downwelling subsurface irradiance or as derived from (Laanen, 2007):

$$R0- = \frac{\pi * \frac{n^2}{1-r^0} * (L_{water} - \rho * L_{sky})}{E_{sky}} \tag{2.1}$$

Where $r^0 = 0.021$ for a $0°$ angle of incidence and $n = 1.341$ for ocean waters and $n = 1.333$ for freshwaters (Dekker, 1993). $\rho = 0.028$ (Mobley, 1999).
The subsurface reflectance $R(0^-)$ is found to be convenient for use in water quality measurements with remote sensing (Dekker, 1993).

Table 2.1: An overview of the symbols used in the equations in Section 2.1

Symbol	Description	Units
E_{sky}	Downwelling irradiance (at depth 0+)	Wm^{-2}
E_{water}	Upwelling irradiance (at depth 0+)	Wm^{-2}
θ	Solar zenith angle	degrees
L_{sky}	Downwelling radiance	$Wm^{-2}sr^{-1}$
L_{water}	Upwelling radiance	$Wm^{-2}sr^{-1}$
K_d	Diffuse attenuation coefficient E_{water}	m^{-1}
$bb776$	Backscatter at 776 nm	m^{-1}
n	Refraction index [1]	-
ϕ	Azimuthal angle	degrees
ρ	L_{sky} correction (Mobley, 1999)	-
r^0	Fresnel coefficient (incidence angle correction) 0° [1]	-
R_{0-}	Sub-surface reflectance	sr^{-1}

From Water Reflectance to Water Quality Parameters

The subsurface light field is indirectly indicative of water quality at a given area. For deriving the afore mentioned parameters which have the most importance (CHL and TSM) a manifold of equations and models have been constructed. For MERIS images equations have been published by Gons (2005) and revised by Simis (2006) amongst others. For this research the algorithms by Gons (2005) and Simis (2006) will be used as these models have also been tested to work with MERIS images with similar band configurations as those taken with the wicam. The theory for deriving TSM and CHL is based on the theory for measuring the light field from above the water surface and relating this to under water reflectance spectra $R(0-)$. There is a difference in calculating the concentrations from $R(0-)$. Chlorophyll-a has very distinct absorption features (e.g. see Figure 2.2). It has to be noted that for estimating CHL the absorption features at $676nm$ are being used in the algorithms rather than those in the $400--500nm$ range, because in this region there are a lot of other features disturbing the signal, e.g. CDOM and TSM. Suspended Matter can mainly be derived from the scattering spectra.

Among the inputs to derive Chlorophyll-a is the backscatter at 776 nm ($bb776$)

$$bb776 = 1.61 * \frac{R(0-)_{776}/(\frac{n^2}{1-r^0})}{0.082 - 0.6 * R(0-)_{776}/(\frac{n^2}{1-r^0})} \quad (Gons, 2005) \quad (2.2)$$

Chlorophyll

$$chl_a(\mu g/l) = \frac{\frac{R(0-)_{708}/(\frac{n^2}{1-r^0})}{R(0-)_{665}/(\frac{n^2}{1-r^0})} * (0.7 + bb776) - 0.4 - bb776^{1.06}}{0.016} \quad (Gons, 2005)$$

$$(2.3)$$
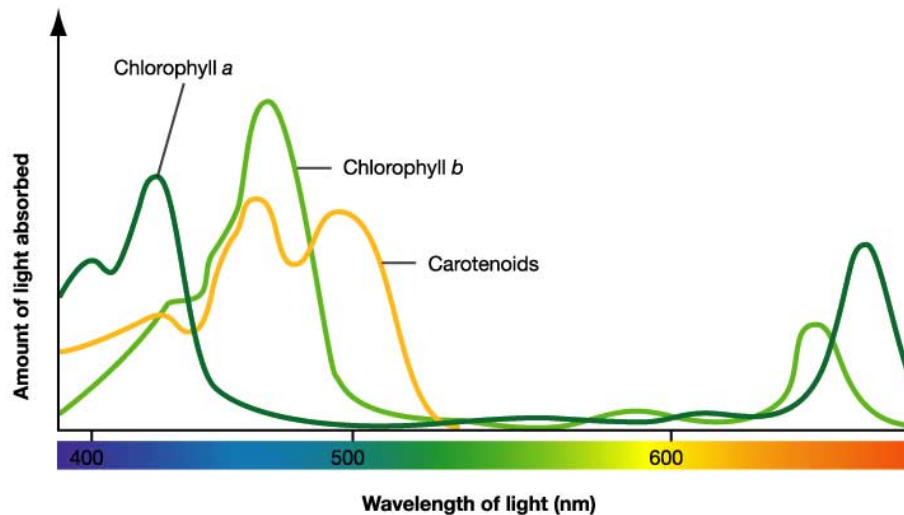
Figure 2.2: Different Chlorophyll absorption spectra. Source http://dedunn.edublogs.org

TSM

$$tsm = 3.818 * \frac{R(0-)_{708}}{R(0-)_{665}} + 200.9 * R(0-)_{708} - 0.93 \tag{2.4}$$

2.2 Geometry, Radiometry (and Illumination) Errors

Raw images can contain any number of errors concerning geometry or radiometry. The geometry concerns the shape of the image and the radiometry concerns values of the measured reflectance as opposed to the actual reflectance. The geometry of the real surface it is photographing might be triangular or trapezoidal, but due to the inclination of the sensor it just looks like a perfectly rectangular block. Geometrical correction comes down to stretching and reshaping the image to represent the real world shape of the observed object. Radiometric errors are more complex, as they can be attributed and resolved in a large variety of ways. The most common radiometric error is that of atmospheric influence. Infintesimally small objects that float in the air (e.g. gases or microdust) and water vapor are largely resposible for scattering of this kind. This may result in too high or too low values of reflection.

2.3   Measuring Instruments

For a Deltares project the WICAM has been mounted at the Marina Barrage in Singapore (see Figure 2.3), this is also to test how the WICAM works in practice.

(a) Location in Singapore

(b) Location with different viewing angles of WICAM
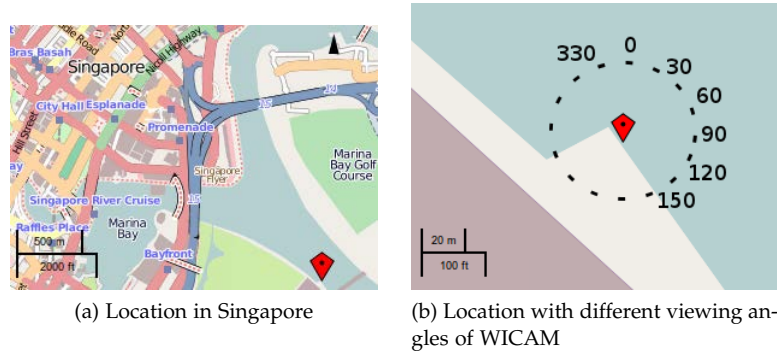
Figure 2.3: Marina Barrage in Singapore

The measurements will be taken continuously throughout the day for 7 viewing angles as seen in Figure 2.3b (7 images x 7 bands + 7 measurement per half hour).
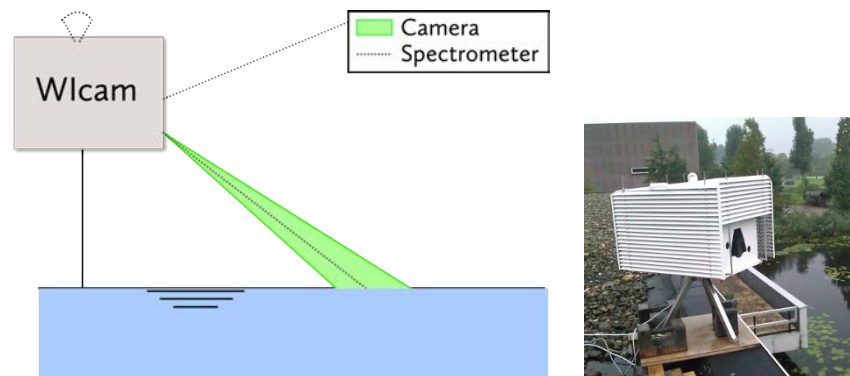
(a) The WIcam takes a spectral photograph simultaneously with 3 different spectrometry measurements. Two for downwelling (ir)radiance and one for the radiance of the water surface.

(b) WIcam mounted and ready for measuring.

Figure 2.4: The WICAM is an optical measuring device with 3 spectrometers and a spectral camera.

WICAM

The WICAM (see Figure 2.4) contains three spectrometers (WISP-3) and a spectral camera (Spectrocam), taking measurements in the configuration showed in Figure 2.4a. The spectrometer and the CCD camera start their measuring

sequence simultaneously. For the CCD camera this means one image for each of the 7 filters. The WICAM as a whole then rotates in the horizontal plane and takes the next measurement with a slight overlap in the image. In total this is done for 7 horizontal rotation angles (as displayed in 2.3b).
The following two sections will describe the device in detail.

Spectrometer

The spectrometer (see Figure 2.5) is a calibrated 3 channel spectrometer built on the JAZ-system developed by OceanOptics; a modular spectroscopy unit (see Figure 2.5a). This particular configuration consists of a battery unit, an ethernet unit, a display processing unit (DPU) and three spectroscopy units. The light unit in Figure 2.5a is optional and can be used in active spectroscopy, but is not used in this configuration. The spectroscopy units are connected to fiber optical cables. The stack of spectrometers simultaneously measures up-welling (L_{water}) and downwelling radiance (L_{sky}) as well as the downwelling irradiance (E_{sky}). For the radiance measurements the fibers are connected to Gershun tubes (see Figure 2.5b). The Gershun tubes are cylindrical tubes which can be used to limit the FOV (Kirk, 1994)], in this case to $1 - 3°$. For the irradiance measurement the fibre optical cable is connected to a cosine collector, which simulates a round sphere, so that the incoming light can be measured from all directions.

(a) An example configuration of the JAZ, a modular spectroscopy unit by OceanOptics.

(b) Fiber optical cable connected to a Gershun tube. Different apertures can be installed for different sensitivities.
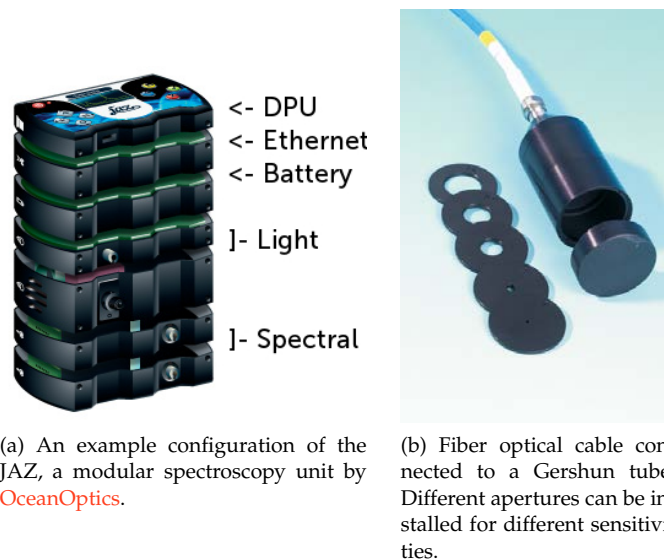
Figure 2.5: Different parts of the spectrometer installed in the WICAM

The spectroscopy units consist of a 2048-pixel CCD Linear sensor (the Sony ILX511B, the area on which the rainbow is projected in Figure 2.6a) connected to a fiber optical cable (connected to cutout in Figure 2.6a). The sensitivity of the sensor is the best in the visible (VIS) and Near Infrared (NIR) part of light.

(a) Insides of JAZ spectroscopy unit.   (b) CCD Camera with revolving filter
                                              source: http://spectrocam.com

Figure 2.6: JAZ and SpectroCam

The spectral resolution, how many wavebands per pixel, depends on the slit (2 in Figure 2.6a), the grating (5 in Figure 2.6a) and the sensor. In the case of the WISP the slit for downwelling irradiance (E_{sky}) is 100 μm and for the radiance measurements (L_{sky}, L_{water}) 25 μm with a #2 grating. The grating, a prism, limits the spectral range to about 600 nm and grating #2 gives it a more sensitive peak in the blue part of the spectrum. As can be seen in Figure 2.6a, the grating (5) determines how the light is diffracted on the mirror that reflects the light to the sensor. The material and the angle of a grating thus determines which part of the light spectrum goes to the sensor. The slit is limiting the amount of pixels that are assigned to a waveband. The wider the slit the lower the spectral resolution is and vice versa. With a $25\mu m$ slit the amount of pixels per waveband ≈ 4.2 according to OceanOptics. With the $25\mu m$ slit and the #2 grating the spectral resolution can be calculated as follows: $(grating/sensor resolution(pixels)) \times slit pixels$ which gives: $(600nm/2048) * 4.2 \approx 1.23nm$. The spectrometer is configured to be sensitive for light among the wavelengths: $195 - 895nm$.

The calculations for converting the raw DN values as the spectrometer measures them to real radiance values is :

$$L_{sky}[n] = \frac{0.01}{2 * \pi * \left(1 - \cos \frac{3^\circ}{2}\right)} * \frac{counts\_sky[n] * calibration\_sky[n]}{\frac{int\_time\_sky}{1000000} * \left(\pi * \left(\frac{0.04}{2}\right)^2\right) * \frac{wvl\_sky[n+1] - wvl\_sky[n-1]}{2}}$$
(2.5)

$$L_{water}[n] = \frac{0.01}{2 * \pi * \left(1 - \cos \frac{3^\circ}{2}\right)} * \frac{counts\_water[n] * calibration\_water[n]}{\frac{int\_time\_water}{1000000} * \left(\pi * \left(\frac{0.04}{2}\right)^2\right) * \frac{wvl\_water[n+1] - wvl\_water[n-1]}{2}}$$
(2.6)

$$E_{sky}[n] = 0.01 * \frac{counts\_irradiance[n] * calibration\_irradiance[n]}{\frac{integration\_time\_irradiance}{1000000} * \left(\pi * \left(\frac{0.39}{2}\right)^2\right) * \frac{wvl\_irradiance[n+1] - wvl\_irradiance[n-1]}{2}}$$
(2.7)

The reflectances, calculated with equation 2.1, are using the calibrated radiances, not the raw DN values.

Spectrocam

The 2D CCD camera (Figure 2.6b) is a device developed by Ocean Optics with a Revolving filter which can revolve with a speed up to 14,000 RPM. The lens can be replaced with another kind of lens, similar to the ones that are mounted on a Digital Single-lens Reflex camera. This gives a variable FOV depending on the lens between $20° − 60°$. The images taken with this device resemble the images taken with several bands similar to those configured on the MERIS sensor. The MERIS images were also used at Water Insight for water quality calculations and were so chosen because the MERIS sensor on-board the ENVISAT was very suitable for oceans and other large open waters because of its narrow bandwidth at interesting wavebands (Kallio and Pulliainen, 2005). Those bands are chosen to pick up features interesting for water quality parameters in complex waters. The filters chosen for the camera are shown in Table 2.2. This shows that one important band ($776nm$) used for calculation of $bb776$ (see Equation 2.2) is missing from the configuration. For this purpose bb776 in the calculations was set to 0, which according to experts at Water Insight is not uncommon as the calculations sometimes gives a negative number and is then also given the number 0. Still, it remains incorrect. For comparison purposes it would have to do.

Each filter has a peak bandwidth of about $15nm$ around the target wavelength. Every image has a pixel resolution of 1392 x 1040. The sensitivity per band is shown in Figure 2.7, note that the curve is for a certain intensity of light. The digitized number values (DN) of the camera are all processed with the same gain factor but have differing integration times. This is highly variable due to the total incoming light and the time it takes to have enough light in an image. The DN values have to be divided by the integration time for comparison purposes.

The images taken with the spectrocam are directly related to L_{water}. This means that after linear model derivation the DN values can be converted to L_{water} measurements, with the use of the Spectrometer L_{water} as a reference. These are then be used to calculate the $R(0−)$, with Equation 2.1 together with the L_{sky} and E_{sky} measurements. After this the $R(0−)$ values can be calculated to concentrations, with Equations 2.3 and 2.4, much the same as would be the case with the Spectrometry measurements. Every pixel is then considered as one Spectrometry measurement.
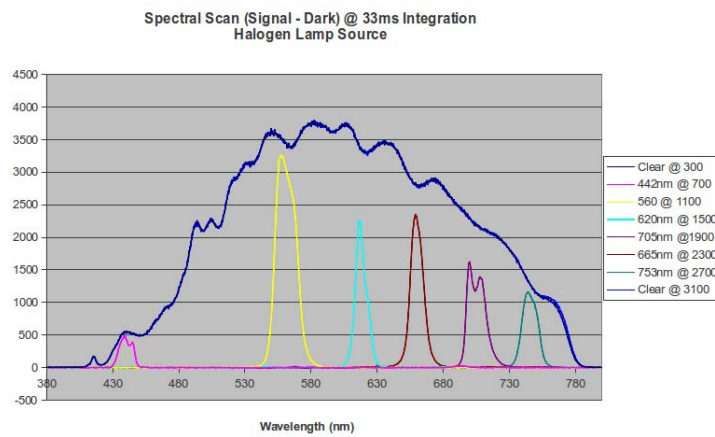
Figure 2.7: Spectral Sensitivity per band of the SpectroCam

Table 2.2: Different waveband configurations for the Spectrocam

Wavebands	Interesting for	MERIS band
$--$	Clear filter	Panchromatic
$442nm$	Blue	2
$560nm$	Suspended solids (soil particles, detritus etc)	5
$620nm$	Cyanbacteria and green-blue algae	6
$665nm$	Chlorophyll-a	7
$705nm$	Start of Near infrared	9
$753nm$	Near infrared	10

2.4 Problem

Combining both the hyperspectral and the spectral image information is valuable as it can describe the optical properties of water with a high spectral and spatial resolution. From these measurements important water quality parameters, total suspended matter (TSM) and chlorophyll (CHL), can be derived with high spatial, temporal and spectral resolution. However, combining these measurements is complex as the two instruments give very different representations of the measured area. To be able to correlate the two measurements, the measurements of the spectrometer need to be localized within the images taken with the camera and compared.

The measurements of the water surface are strongly influenced by surface roughness i.e. waves, and different lighting conditions for different measurement sequences. The time interval between the measurements are likely to have a pronounced effect due to the change in surface roughness and therefore conditions of the light interacting with the water surface.

The comparison therefore needs to define these sources of variability. Hereafter the images can be filtered on variability parameters, thus minimizing the variability between the measurements.

2.5   Research Question

How can high resolution spectral point data and spectral 2D images be integrated to provide one product for deriving water quality parameters?

Sub-questions

- How do the different measurements of the WICAM, i.e. the camera and the spectrometers, correlate in the corresponding pixels?

- What is the main source of variability between the measurements?

- How can the variability be minimized?

- How can the two measurement types be integrated?

Chapter 3

Methods

The methods of this research are explained in this chapter. Figure 3.1 gives an overview of all the steps that are taken to come to results. The flowchart only gives a short overview, the rest is explained in this chapter. The flowchart can be explained as follows: the WICAM device takes a measurement that comes out as stitched together file. This stitched file is taken apart in the preprocessing, together with filtering. The measurements once extracted are stored in a *CouchDB* database. Different subsets of the camera pixels are stored and calibrated spectrometry measurements are stored. From the database it is easier to calculate and store other things like a linear model and reflectance values, to relate the camera pixels to reflectance values. Because the camera images were found to be quite noisy, an extra median filter has been applied for better results. After the reflectances are calculated the reflectances serve as input for the water quality models to end up with an integrated water quality product.

3.1 Preprocessing

Before the actual calculations and intercomparison were started the data needed to be prepared and filtered. As decribed in more detail before, the spectrometry data has 3 raw spectra per measurement with 2048 pixels describing wavelengths from 295 – 895 nm. The spectral images have 7 bands, 6 with filters with 1392x1040 pixel resolution. The whole dataset consists of 1345 measurement sequences taken between the 23th of December 2011 and the 2nd of January 2012. The flowchart in Figure 3.1 gives an overview of all of the steps in the methodology and where "Preprocessing" fits in.
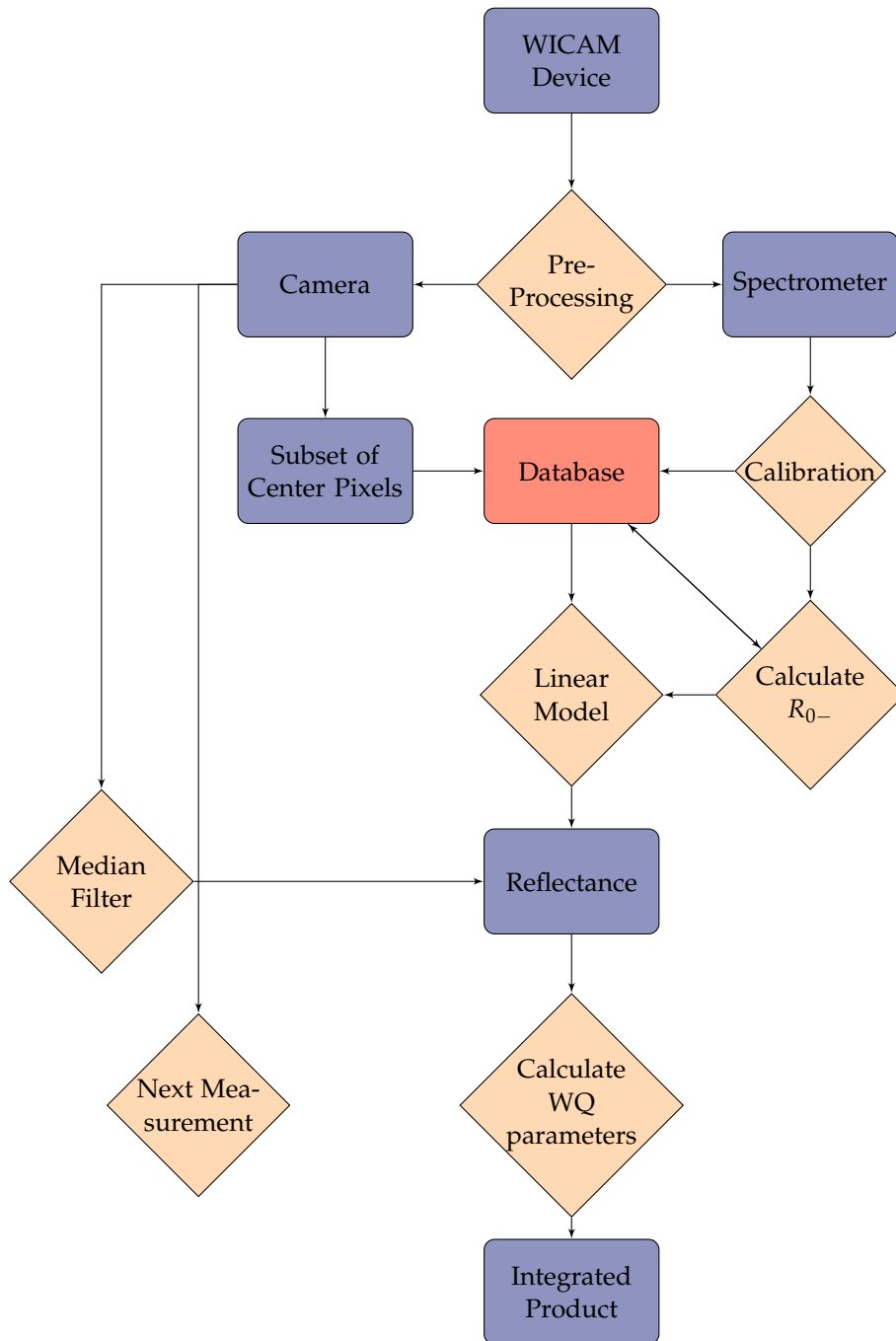
Figure 3.1: Flowchart of methodology.

Filtering the Data

Part of the preprocessing was making different categories of how "good" or useful the measurements are. This depends on a few criteria. According to Gons (2005) and Mobley (1999) the azimuthal angle of the spectrometry measurements from the sun have to be at $90°$ or at an optimum of $135°$ respectively. This is due to the effect of sunlight reflecting on the water surface, especially when measuring with a zenith angle of around $42°$ which the WICAM is doing. Thus, the measurements will be filtered to remain with measurements with an azimuth angle between $90°$ and $135°$ from the sun. Because the high sun altitude in Singapore these requirements become of less importance. When the sun has a higher solar elevation angle than about $50°$ the light does not reflect on the surface directly as it does with lower solar elevation angles (see Figure 3.2a for the result of sun glint in the images). The symbols of the following equations are explained in Table 3.1.

Table 3.1: An overview of the symbols used in the equations in Section Filtering the Data

Symbol	Description	Units
ϕ_s	Azimuthal angle	degrees
θ_s	Solar zenith angle	degrees
h	Hour angle of the present time	degrees
δ	Current sun declination	degrees
Φ	Local latitude	degrees

Calculation steps are:

1. Calculate sun's azimuth for time of day, day of year and place on earth:

$$\cos \phi_s = \frac{\sin \delta \cos \Phi - \cos h \cos \delta \sin \Phi}{\cos \theta_s \cos \Phi} \tag{3.1}$$

2. The azimuth angle of the sun relative to the measuring direction of the WICAM:

$$\phi_{sw} = \phi_s - \phi_{wicam} \tag{3.2}$$

A negative ϕ_{sw} signifies an angle to the left of the ϕ_s angle and a positive value an angle to the right.

Measurements during rain also have been filtered out, because the images taken by the camera become smudged due to droplets on the lens (see Figure 3.2c). Moreover the rain distorts the water surface and the incoming light. This filtering was done by hand, but might in the future be automated with rain sensors. Measurements containing lots of shade, like Figure 3.2b, can not be used. These also had to be selected by hand.

(a) WICAM image with
sunglint

(b) WICAM image with lots
of shade of the Barrage

(c) WICAM image with rain
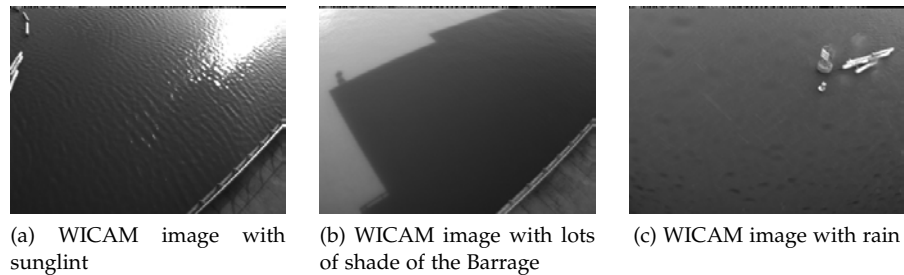
Figure 3.2: Different WICAM images that cannot be used.

Preparing the data

After being selected and filtered the data needed to
be prepared in a format that can be used by GIS soft-
ware. The data comes in as a composite tiff, with all
of the seperate bands stitched together as one image
as shown in Figure 3.3, not as a multiband file, like
common raster images. The metadata and the raw
spectra of the WICAM are saved in a text format
which also has been stitched as a binary image. The
images have been cropped and stacked, in the Geo-
TIFF format, as a multiband image. The metadata
file has been unpacked and stored together with the
spectra in an XML-file. For the spectra a number
of calculation steps are necessary. The raw spectra
have calibration files that define mapping of the raw
counts as being part of particular bandwidth ranges.
After this the counts needed to be converted to radi-
ance/irradiance values after which reflectance val-
ues could be calculated.

The calculation steps for this involve equations
2.6, 2.5, 2.7 and 2.1.
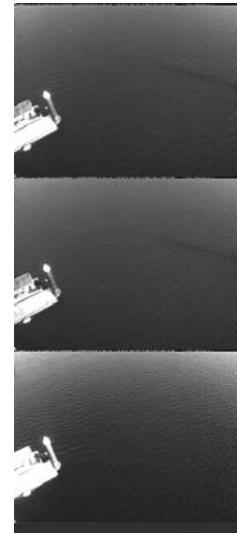
Figure 3.3: Composite
image, shows the meta-
data and spectra in the
bottom

3.2   Relating the WICAM images to the spectrome-
try measurements

The spectrometry measurements after preprocessing give reflectances and
(ir)radiances values of the measurements. The digital number values of the
camera had to be related to L_{water}. For most earth observation products there
is a linear relationship between the reflectance and the DNs (Karpouzli and
Malthus, 2003).. The linear modelling showed this clearly.

The footprint of the spectrometer in the image, the measured area of the
spectrometer that corresponds to the pixels in the spectral image, has been

compared with the measurements of the spectrometer. Firstly, to find out which pixels best correspond to measured reflectances with the spectrometer. Secondly, to find out how they relate spatially, and to what extent the point measurement can be used to validate the rest of the pixels.

For the comparison different sizes of image subsets have been used to see to which subset the spectrometer best compares.

3.3   Variability sources

The variability between the correlations of the images and the spectrometry measurements will be inspected to attribute the variability to sources such as:

- irradiance conditions, related to incoming light and time of day

- surface roughness of water

- dependance on viewing angles

The variability and correlation of the spectral images will be investigated amongst the different spectrometry measurements (L_{water}, L_{sky} and E_{sky}) and amongst the different wavelengths with least squares regression.

3.4   Integration of the two measurement types

The radiance values calculated with the derived linear model can be used to calculate the reflectance values over the whole image. The further away from the center of the spectral measurement within the spectral image the lower the correlation will be to the spectral measurement. Extrapolating the correlation of the footprint of the spectrometer to the rest of the image will therefore mean introducing a certain amount of error.

Because the images are taken in a sequence there is some overlap (see Figure 3.4). The correlation amongst images could thus be assessed

Figure 3.4: The images have some overlap. The spectral measurement therefore also has correlation with another image in the sequence.

with the calculated reflectances and the spectrometry measurements in the next or previous image in the sequence. For every measurement that falls within the filtered images the images that are next to each other and taken within one sequence of images have been compared. The correlation between spectrometry meausurements with other spectrometry measurements in the frame next to it and the DNs and the spectrometry measurements and the DNs and the DNs have been compared.

Chapter 4

Results & Discussion

"[They] agreed that it was neither possible nor necessary to educate people who never questioned anything."

Joseph Heller

This chapter is organized as follows: first the results of both the devices, spectrometer and camera, are analysed individually. Subsequently the results of the device as a whole, the WICAM, are shown to compare and identify the main sources of variability. The measurements of the device will be integrated to be able to output water quality products that can be derived using such a device. The results hereof will add to the discussion of the use and variability of the device.

4.1   Overview of the data

The WICAMs measurements of 23 December 2011 – 02 January 2012 were evaluated in this study. The whole dataset consists of 1345 measurement sequences, of which 500 measurements were deemed fit according to the first filtering step based on solar azimuth (also see Table 4.1). As the solar azimuth takes care of the sun being behind the sensor most of the glint was filtered out. However, still a few images with glint remained and were filtered out. A few measurement sequences were taken during rain showers and were taken out of the dataset. After removing measurements with little water pixels (Angles 120°, 150° and 330° shown in Figure 4.1) 283 valid measurements remained. After the preselection there were unforeseen outliers that propagated into the regression analysis, which were therefore also taken out of the subset, leaving the subset at 281 valid measurements. These outliers were a measurement taken during the night (but still in compliance with the solar azimuth angle criterion) and a measurement with a boat in the place where the spectrometer was measuring. Some of the unsuspected anomalies are pictured in Figure 4.2.

Table 4.1: Overview of measurements with the different filters, describing how many measurements are left after each filter.

Filter	Amount of measurements
No filter	1345
Solar azimuthal angle	500
Little water pixels	318
Rain and glint	283
Boat	282
Night	281

(a) Angle 330°	(b) Angle 0°	(c) Angle 30°	(d) Angle 60°

(e) Angle 90°	(f) Angle 120°	(g) Angle 150°
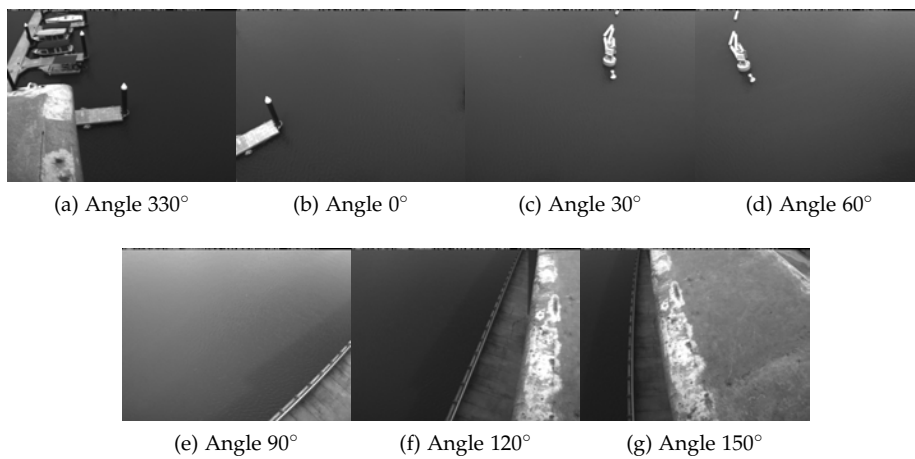
Figure 4.1: Example sequence of images taken with the WICAM with the clear or panchromatic filter on the 1st of January 2012 at 5:30 AM - UTC time

(a) Measurement at night.	(b) Measurement with a boat.
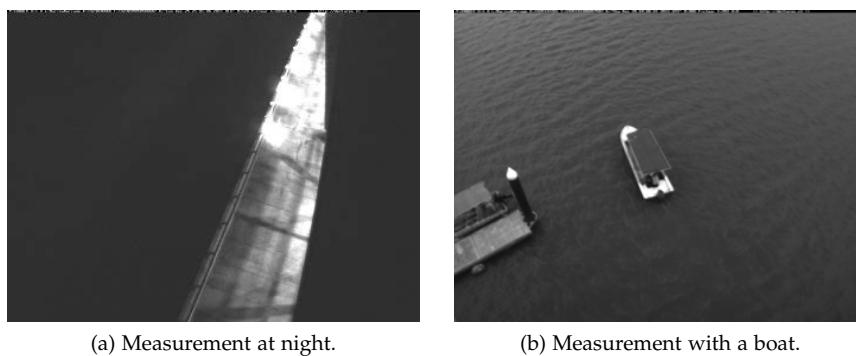
Figure 4.2: Images that were surprisingly erroneuous, compared to the rest of the dataset.

Camera

The measurements taken with the camera have 7 different viewing angles. These are displayed in 4.1. The camera's measurements have noise in the images. This can be seen in Figure 4.3 where the images per band are shown. The panchromatic image is very clear and sharp but the individual bands are noisy.

(a) 442 Filter

(b) 560 Filter

(c) 620 Filter

(d) 665 Filter

(e) 705 Filter

(f) 753 Filter
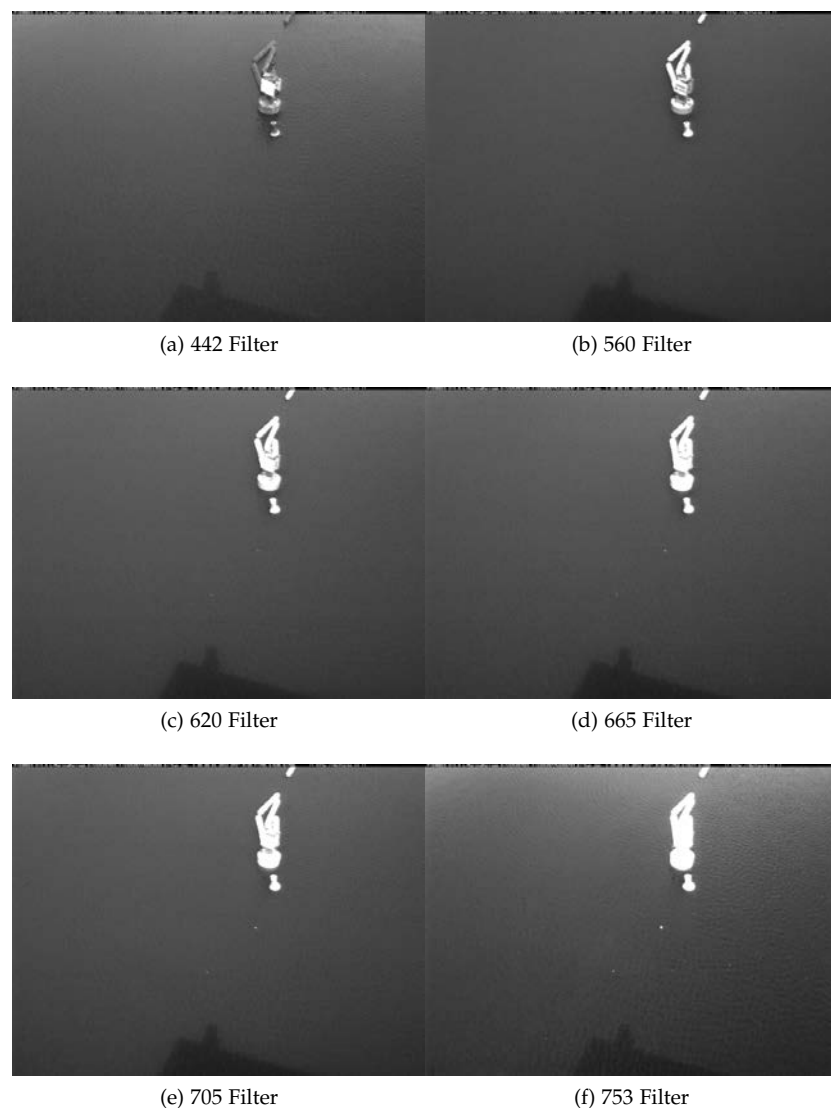
Figure 4.3: Example images in the different bands configurations.
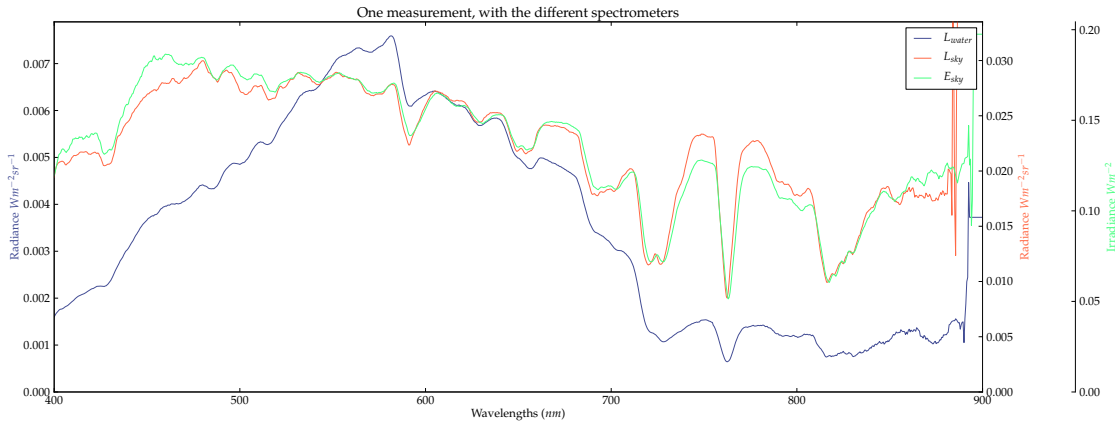
Figure 4.4: Example measurement of the 3 spectrometers.

(a) 20 random L_{water} measurements

(b) 20 random L_{water} measurements zoomed in
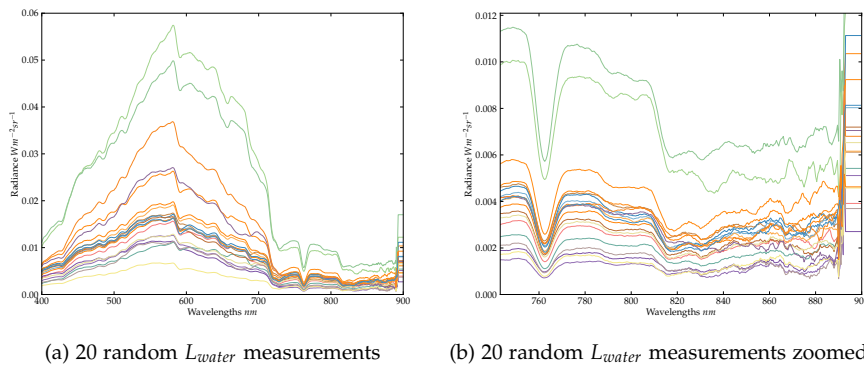
Figure 4.5: Some L_{water} measurements to show different interesting spectral features in the high quality spectrometry measurements.

Spectrometer

An example of the spectrometry measurements of the three different spectrometers can be seen in Figure 4.4. The spectrometers that measure E_{sky} and L_{sky} give a very similar pattern but are in a different range (see Y-Axes), one is irradiance, one radiance, which might lead one to think of leaving one of the two spectrometers out. This would be false as will be made clear in Section 4.4. This is a measurement which complies to all of the filter rules, i.e. right solar angle, no glint, no rain etc. Furthermore, the signal the spectrometer is able to measure becomes noisier towards the edges of its spectral range. This can be seen in Figure 4.5. In this area the most interesting part is the use of the backscattering coefficient at 776 nm (or bb776 in equation 2.2) just after the absorption dip. Other areas of interest are around 665 nm and 753 nm as they serve as input for the calculation of TSM and CHL according to equations 2.3 and 2.4. The large difference between measurements in the 400 to 600 nm re-

gion is likely due to a rainfall event. After the rainfall event the measurements had a higher slope and a higher peak around this region, which is often indicative of high concentrations of suspended sediments, which start floating to the top after rainfall events (IOCCG, 2000).

4.2   Correlation between the spectral camera and the spectrometer

The measurements of both the spectrometer and the camera have been filtered according to the filters of the methodology. Glint, rain, shade and uninformative azimuth angles of the sun have been filtered out of the dataset. The filtered measurements of the different spectrometers were compared with the images to compare how the three spectrometry measurements and the spectral imagery relate. Different subsets of the image were used to do this. The spectrometer measuring water is expected to measure the area around image pixel x: 650, y:600. Around these pixels subsets of different sizes (10,10; 37,50; 50,50; 100,200; 350,500;) have been tested to look at the relationship between the image pixels and the spectrometer. It was found that the size of the subset was not really of much influence on the degree of correlation, as the water body is very unifom in the middle of the images. The smaller subsets had marginally higher correlations with the spectrometer than the very large subset. The 37,50 window most resembled the footprint of the spectrometer and was chosen for the analysis. For every image band (see Table 2.2 for the configuration of the bandwidths per bands) the DNs of the camera and the (ir)radiance measured with the spectrometer were compared with least squares linear regression. The values of the spectrometer were calculated using the corresponding spectral bands and taking the average over a 15 nm bandwidth, because of the peak sensitivity shown in Figure 2.7. The results of these analyses are shown in Figure 4.6 and in Appendix A in Figures A.1 and A.2.

For every band the correlation was different, with the correlation in the bands with visual light being higher than those bands towards the infrared. The images of the different bands are grainy and coarse, showing more noise in bands at 665, 705 and 753nm (see Figure 4.3).

For every spectrometer, the irradiance, the radiance from the sky and the radiance from the water, the correlation with the DNs was different for each seperate band. The spectrometer with the least correlation was the radiance measurement of the sky, L_{sky} shown in Figure A.1. This low correlation in the L_{sky} can be attributed to the very narrow FOV of the incoming sky radiation which should correct for the incoming sky radiation at the exact angle the radiance coming out of the water is measured (also see Figure 2.4a). Because of the narrow FOV the ever changing sky, with clouds and light coming through it, is likely to only hold true for a specific moment in time and a specific angle (precisely the reason why this is mounted in the same angle as the water observing spectrometer). The reason it shows any correlation is due to the

Table 4.2: Results of the regression analysis for different wavelengths and spectrometers

Parameters for correlation	$442nm$	$560nm$	$620nm$	$665nm$	$705nm$	$753nm$
R^2 for L_{water} with DNs	0.997	0.992	0.990	0.972	0.974	0.990
x for $L_{water} = x * DNs$	0.105	0.041	0.120	0.097	0.093	0.130
R^2 for L_{sky} with DNs	0.814	0.672	0.649	0.642	0.639	0.796
R^2 for E_{sky} with DNs	0.920	0.936	0.893	0.869	0.869	0.852

incoming total energy available. If there is more sunlight this contributes to higher radiance and (ir)radiance values.

To relate radiance measurements of the water surface and the camera's DNs the linear slope coefficient is derived, shown in Table 4.2. This coefficient was used to convert the DNs to radiance values. From the radiance values the R_{0-} can be calculated with equation 2.1 which serves as an input for the water quality models for Chlorophyll-a and Total Suspended Matter, equations 2.3 2.4. The correlation between the pixels that feature only water (not other objects e.g. the buoy, or the pier) and the spectrometry measurement was very high, independent of the size of the subset. In Figure 4.6 the correlation between the two can be seen resulting in high correlation. The comparisons with the other spectrometers, which show up in Table 4.2, are plotted in Appendix A.

   Overall the images and the spectrometry measurements are strongly related, with which the values can be converted to the physical reflectance values instead of the DN values. For every image there is a gradient of light because of the inclination angles and the FOV of the camera. This can also be seen in the end result in section 4.4.
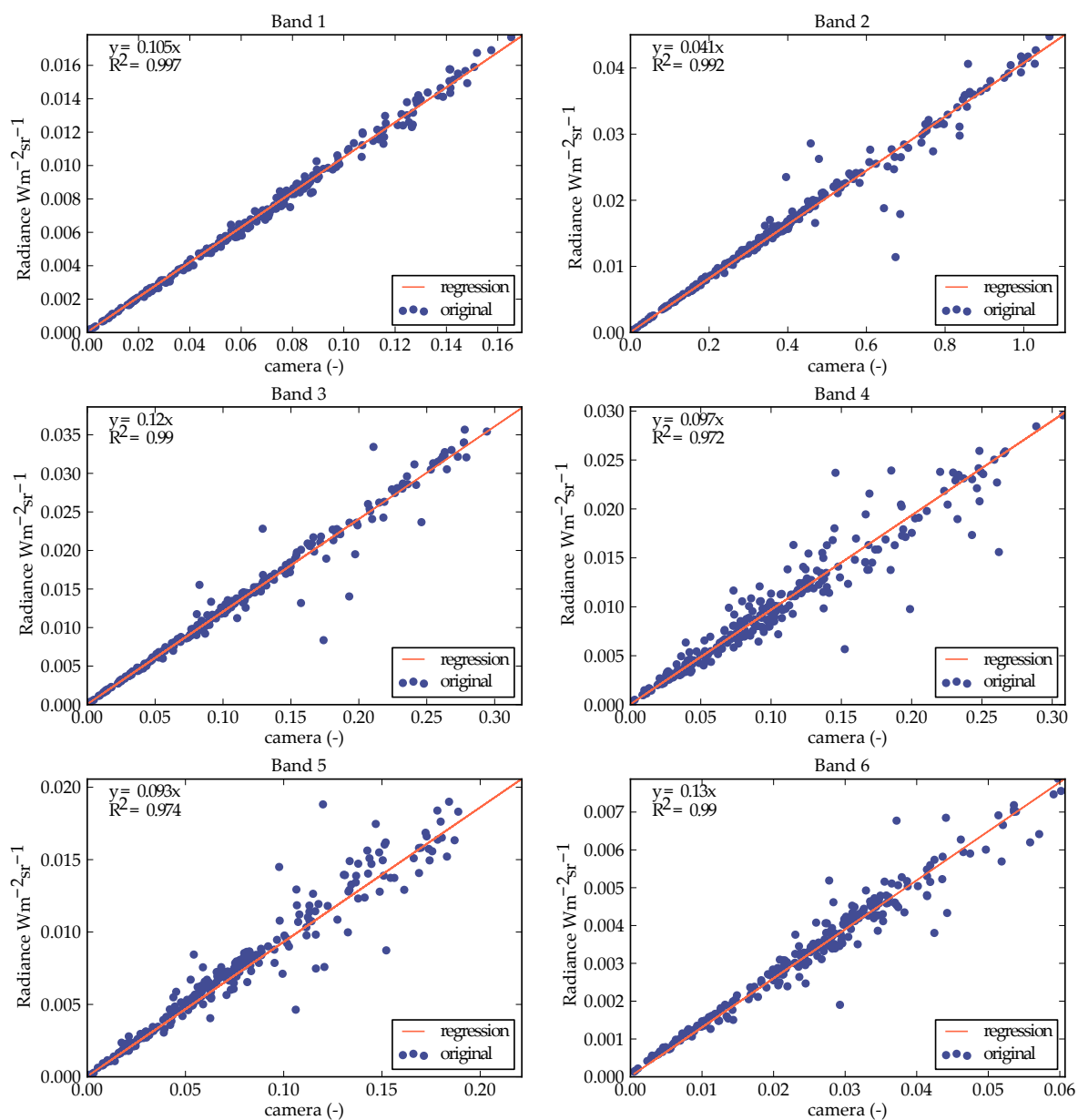
Figure 4.6: Correlation between L_{water} and the DNs of a subset of pixels.

4.3 Explaining Variability

The variability that was found in correlating the camera and the spectrometer
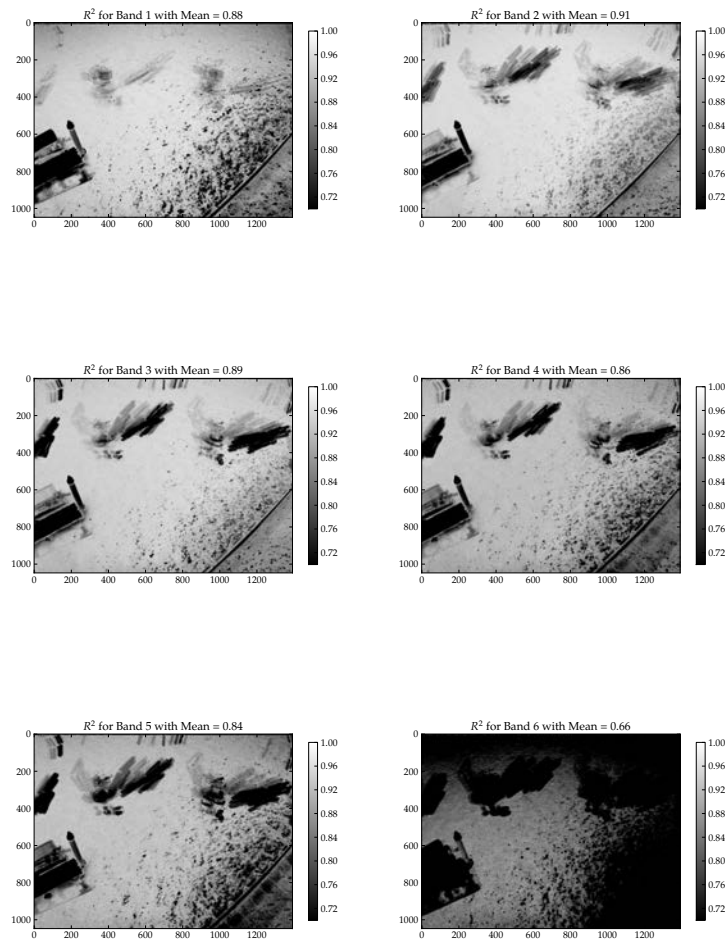
Figure 4.7: Overview of R^2 between all camera pixels and L_{water} measurements.

uniform whereas the features that are not water clearly stand out. Towards the upper edges of each image a gradient can be seen caused by the range of inclination angles because the device is mounted at an angle. The pixels further away from the WICAM device therefore will have a different solar angle and can reflect more light from the sun directly instead of the most optimum angle as derived by Gons (2005). According to Kirk (1984) the relationships between apparent optical properties (AOP) and inherent optical properties (IOP) are significantly dependent on the incidence angle of light. As mentioned in

the Context & Background the IOPs are the properties that are constant and AOPs the properties are subject to change according the angle and amount of light available (Preisendorfer, 1961, 1976). This means that the pixels further away from the WICAM, will return different results than those closer to the device or in the middle of the image. These differences are of special importance when these relationships between AOPs and IOPs are to be established to derive concentrations. This will come back in the section Integrating both measurements.

The value of L_{sky} only holds true for a very specific angle. That is its purpose and its design, to be true for the exact angle in which L_{water} is measuring. To extrapolate to the rest of the image is therefore not advised. This can be deduced beforehand by reading the design of the spectrometers setup and the theory behind it. However, the fraction of L_{sky} that is being used for the calculation is small and will influence the reflection values $R0-$ in the calculations, but not that much, as $\rho \times L_{sky}$ equals $0.028 \times L_{sky}$. Still the angles specifically chosen for the spectrometer seem not to have been taken in account for the much wider FOV of the camera. The wide FOV that can vary between $20° - 60°$ means that the azimuth angle of the camera on the water surface has a very small surface that corresponds with the proper angles as proposed by Gons (2005). The higher angles give rise to the problem of reflection of the sky on the water surface (Gons, 2005), not really sunglint but sky and cloud features. This is very clear on the images that fall outside the solar angle filter. The calculation of water parameters in images like these becomes useless as much of the water surface is reflecting the sky.

Another consideration concerning the radiance and irradiance measurements
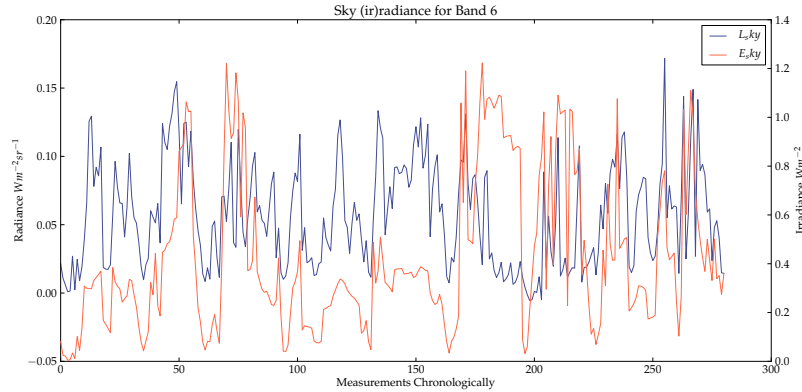
Figure 4.8: Comparison of L_{sky} and E_{sky}.

of the sky is the similarity they show (especially in the example in Figure 4.4). One could think the L_{sky} measurement at the incidence angle of the L_{water} measurement could be derived or modeled from the E_{sky} measurement. In fact modeling can be done (Igawa et al., 2004). However when comparing all of the measurements for one band (see Figure 4.8) it is clear that a simple relationship does not exist.
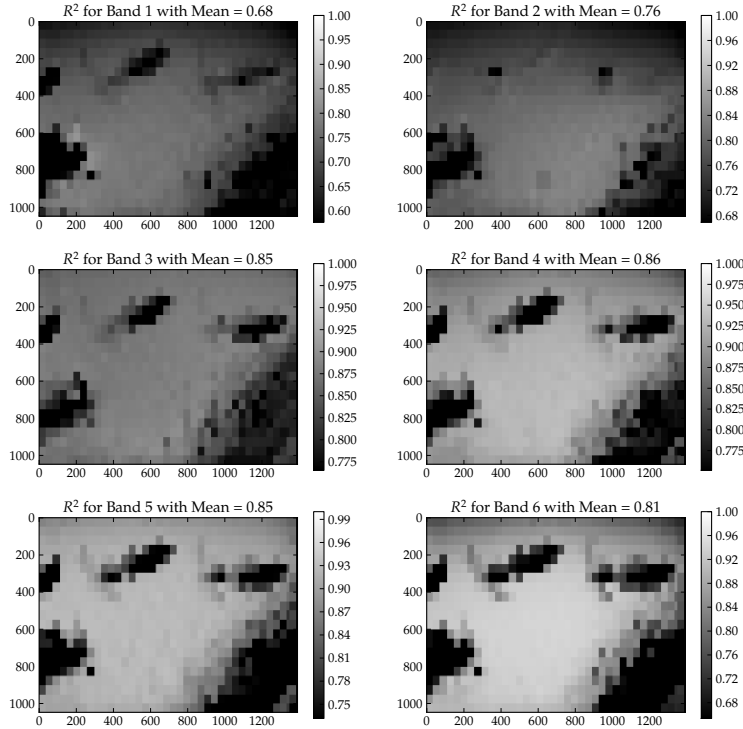
Figure 4.9: Overview of the different bands R^2 per median block comparing all of the images with all of the spectrometry measurements.

A per block assessment of the alignment of L_{water} spectrometry measurements and the images has also been run to investigate the correlation among smaller plots to find out where the spectrometer and the measuring device match best, results shown in Figure 4.9. This was helpful to find out segments where the spectrometer and the camera are best aligned. Figure 4.9 shows the result of the regression of blocks similar to the spectrometers estimated footprint. The median of each block for all measurements within the filter has been analysed. The black blocks are features that are not water and therefore stand out in the analysis. These features are the pier (see Figure 4.1a and 4.1b, the buoy (see Figure 4.1c and 4.1d) and the walkway of the barrage (see Figure 4.1e, 4.1f and 4.1g). In the filter the worst of these measurements were already taken away, angles 330°, 120° and 150°, because in those cases the spectrometer does not measure the water surface at all. The features stand out because the spectrometer measures the water and these values are very different to the other features that are picked up by the camera. These results confirm what has been said before in section 4.2. The results for water pixels and the center

of the image are really good and towards the edges the correlation decreases. This is important as this also comes back in the integration in 4.4. The further one moves away from the center, especially to the top of the image, the lower the correlation becomes.

Another source of variability is surface roughness, or in water bodies: waves. The camera and the spectrometer take the measurements more or less at the same time. However, the integration time and measuring sequence for the spectrometer takes a few seconds more. The camera at that moment is shooting 7 images, with the filter wheel that can manage speeds up to 14,000 RPM. One with the clear filter and 6 with the chosen filter bands. The 7 images cannot be taken simultaneously and when surface roughness of the water is high this can cause problems as the wave forming shade and a light gradient shifts in every subsequent image, see Figure 4.10. This effect is surprising as the time between the first and the last image on average is under 10 secs (see Figure 4.11). The effect it causes can be explained by the bi-directional re-
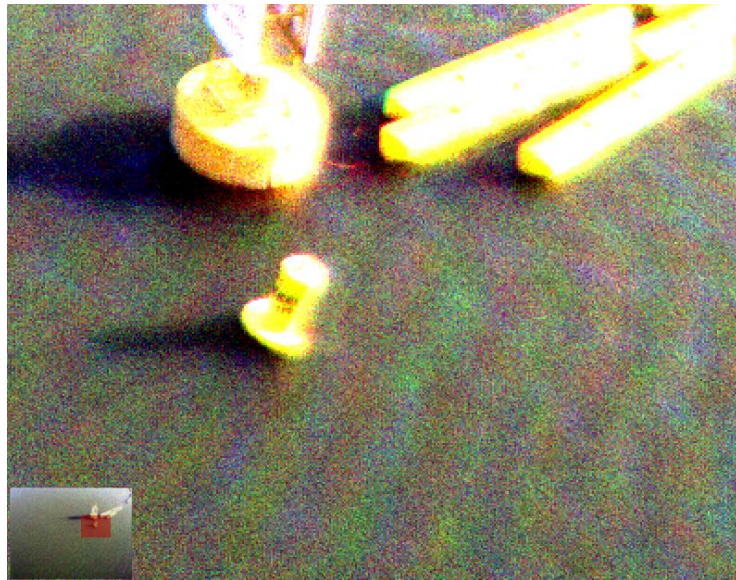
Figure 4.10: Bands 442 nm, 560 nm, and 665 nm in a RGB composite, showing disturbance by surface roughness.

flectance distribution factor (BRDF), describing the distribution of energy that goes to the sensor at different solar azimuthal angles. Because every wave has a slope reflecting light there will be a distribution of the radiation that is dissimilar to a Lambertian surface reflection (Clavano, 2008). The image configured in a threeband RGB image, shows "echoes of a wave" in the next color band. The buoy also looks like a stereograph image. However, the incidence angle of the camera in the images is precisely the same. Koponen et al. (2001) uses wind speed as a parameter in forward transfer models. This is something that has not been done in this research, but would be interesting to investigate further. The multiband image is used for calculation of the concentrations.
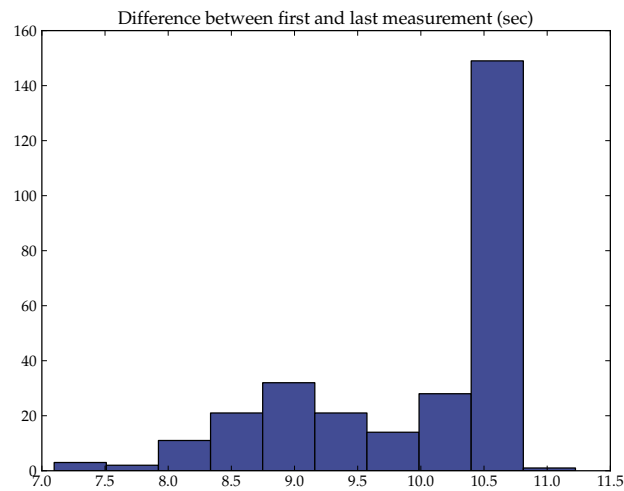
Figure 4.11: Histogram of the differences in seconds between the first and the last image taken in a sequence.

Thus it can lead to miscalculations of concentrations.

Waves do not only distort the multiband image, but also reflect light back from other sources (Torgersen et al., 2001), which is in fact the main cause of variability: Light. The most disturbing and deviant variation is caused by sunlight. This is especially clear in the prefiltering. Most of the images do not even comply to the first filter (see Table 4.1) because the sun light is from the wrong direction. With images that fall outside the filtering the algorithms become less dependable, but still useful. Still, the main cause for disturbance in these kind of images is light.

The overall variability can be attributed to one major source, which manifests itself in different forms: light. This is also clear from the filtering, from the 1345 measurements that are taken in total only 500 (or less than 40%) comply to the solar angle filter. To mitigate the variability caused by light it becomes necessary to look at the setup of the device. The device is setup to be able to rotate in different angles. These angles are now fixed and data that is redundant or unfit for use is still being collected. Using the time of day to calculate the solar azimuth angles to only record the measurements that fall within the correct solar angle filter, could mean a big difference in expenditures in terms of data transfer and data storage costs. The angles that the sun is coming from can be calculated and adjusted for the location, time of day and day of the year. Solar altitudes differ around the world. The device is now mounted in Singapore. This is located at the equator and has very constant solar elevation angles. In e.g. the Netherlands this is not the case, and advice could then be to mount it North facing to have the sun always at your back.

Band 5 Original   Band 5 Median 3   Band 5 Median 5

Figure 4.12: Image (timestamp: 1324870332) the difference between the original and the use of the median filter at a radius of 3 and 5 pixels

Noise and speckle

The resolution of the images is high but the quality is variable as the images have quite a bit of noise and speckle (see Figure 4.12). This can be alleviated through the use of average or median filters. A median filter has been applied to test noise reduction. A fast algorithm to do this is proposed by (Weiss, 2006). The median filter has been run at differently sized radii. See Figure 4.12 for the resulting imagery. The results show a big difference in noise and speckle in the different radii of the median filter. Even a 3x3 window already reduces the noise of the image remarkably. These results are also used in the integration of both measurements to show the difference it makes in the use of the algorithm to have filtered or noisy images.

4.4   Integrating both measurements

The integration of both measurements is twofold, one part is calculating concentrations from the derived L_{water} values taken with the spectral camera. The corresponding pixels of the camera and the image as a whole are considered. This is important as concentrations of e.g. suspended soil particles can differ a great deal, even with small distances (Curran and Novo, 1988). This is the last part of this section.

The other part is investigating the measurements as a whole. The measurements are taken at a certain time and in a sequence. This would mean that one measurement in a sequence has a certain relationship with another measurement in the same sequence.

Correlation amongst the images

Every measurement sequence consists of taking images and measurements in 7 different angles (see Figure 2.3b for the 7 configured angles). As images of one sequence share a part of the FOV both the spectrometer and the camera can be compared with the following or previous measurement in the sequence, see Figure 4.13. If measurements next to each other both comply with the filters described in the Methods (e.g. solar azimuth, no rain etc.) and fall within the same sequence of measurements the one spectrometry measurement can be compared with the next one in the sequence, to get insight

in the consistency of pixel values of the images in different angles, to iden-
tify potential inconsistencies. The measurements that were next to each other
that both complied to the filters were not many: 135. That is only 10% of the
whole dataset. For the DNs of the camera this was also done and showed
very consistent high correlation values, see Figure 4.14. The spectrometer and
the next spectrometry measurement were also quite comparable, although the
distance between these two measurements is significant (also see Figure A.3.
This corresponds with observations in section 4.2, that the water body has very
uniform and comparable reflectance values. The overall variability is mostly
due to the solar angles that change from the closest pixel to the camera to the
furthest. The variability between the images values of incoming light is low
when these pixels are water pixels. This means that integration at an image
to image basis, producing a sequence as a panoramic image with calculated
concentrations would be possible with images that both fall within the filters
and in the time series.
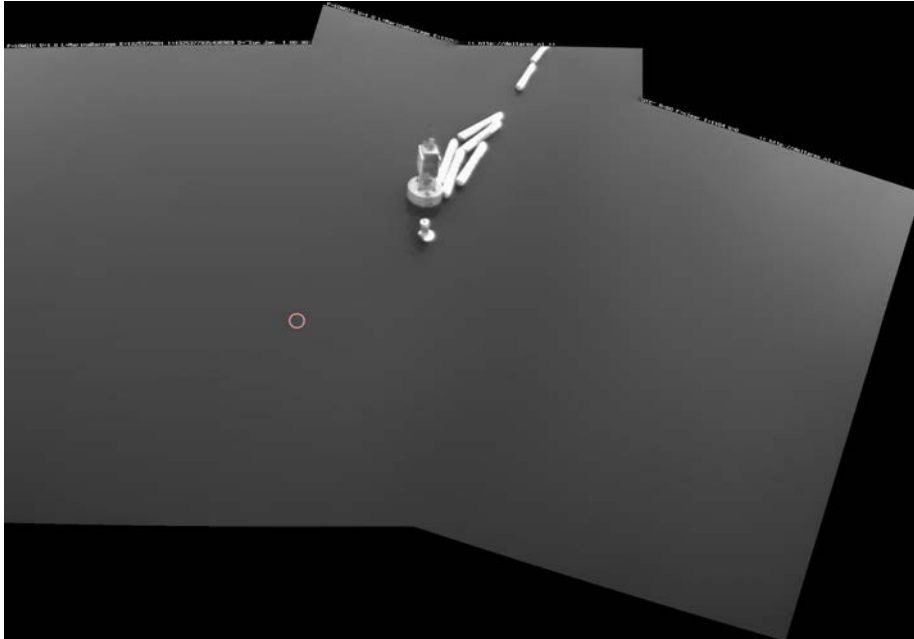
Figure 4.13: Images stitched together to show overlap and location of the spec-
trometry measurement in the following image.
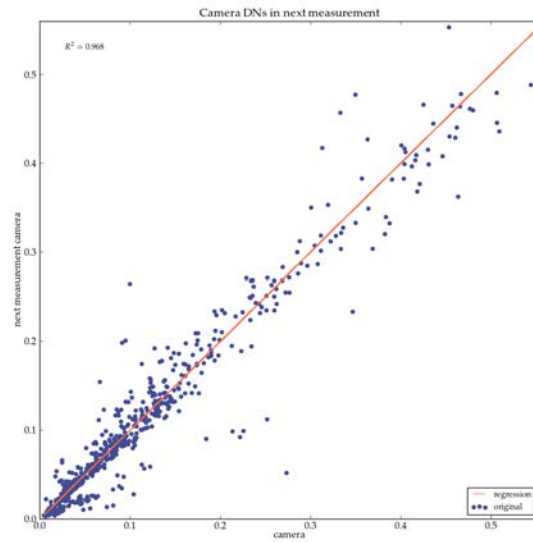
(a) DNs of camera compared with following/previous image next to it
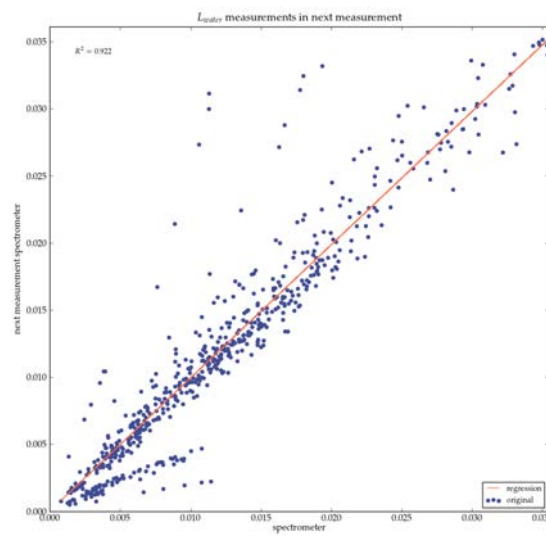
(b) Spectra of spectrometer compared at certain intervals with spectrometry measurement next to it

Figure 4.14: Two correlation plots comparing two different measuring angles which have overlap in the FOV.

Water Quality

To be able to say something about the water quality at the Marina Barrage, where the WICAM is mounted, the concentrations for Chlorophyll-a and Total Suspended Matter have been calculated using the images after converting the DNs to $R(0-)$ values. The conversion from DNs to $R(0-)$ is using the spectrometer E_{sky} and L_{sky} values as well as the camera DNs converted to L_{water} based on the linear slope coefficient derived in the correlation calculations in section 4.2 in Table 4.2. A few maps are shown that were produced with equations 2.3 and 2.4.

The images reflect the afore mentioned remark about the L_{sky} measurement only being valid for a very specific zenith angle to the sensor. This is exemplified especially in the TSM map in Figure 4.17, more on this later. The gradient of the concentration is unlikely to be true. It is most likely attributable to the gradient of light towards the sensor.

The equations 2.3 and 2.4 both depend on the bb776 factor which in turn depends on $R(0-)_{776nm}$. This band is not featured in the camera filters. The band is derived by Water Insight by using other bands, but these bands are also missing from the configuration. Without the bb776 the calculation becomes a bit different. It can still be executed with setting it to 0. This does not make the results of the maps very reliable, it now remains more of a direction in which these products could go. The difference between using bb776 or not having it available is shown in Figure 4.15. This is done with the use of the spectrometer only as the spectrometer also measures in the 776 nm region. The bb776 calculated can in theory be used to calculate the CHL parameters for the camera, extrapolating the value of bb776 at one specific location, to the rest of the image. This was not something that was done in the maps produced at the end of this chapter.

The results of the images have been used to plot the concentrations compared with the concentrations as the spectrometer would calculate them (see Figure 4.16). The TSM as calculated using the camera in combination with the spectrometry measurements is very comparable to the TSM concentrations that are calculated using only the spectrometers. However, the CHL concentrations calculated from the camera pixels converted to L_{water} do not follow the same pattern. This may be explained through multiple effects. According to literature it is commonly found that the TSM parameter is easier to detect with optical instruments than other parameters (Ruddick et al., 2008). The parameter CHL is found to be linearly related to the absorption (Tanaka et al., 2004) at more specific wavelengths (Gitelson and Merzlyak, 1996), opposed to TSM which has an almost linear relationship with scattering at any low to midrange wavelength reflectance (Ruddick et al., 2008). However, detection of CHL can be in much subtler colour hues requiring high quality optical instruments (such as the spectrometer) (Ruddick et al., 2008). This is also seen in the graph in Figure 4.16. From the trends it can be concluded that the spectrometer and the camera are compatible for detecting TSM. For CHL the results do not look as promising.
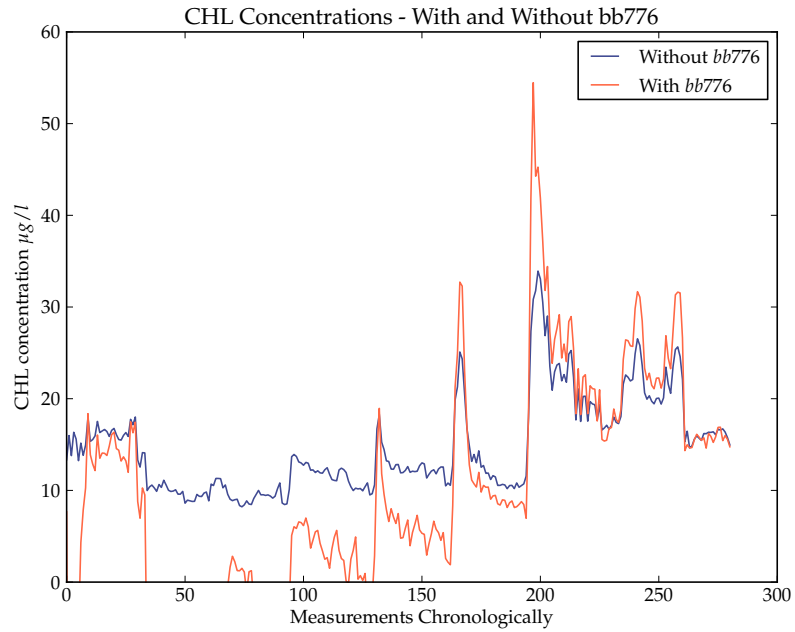
Figure 4.15: Difference between calculations for CHL with and without the use of the bb776 parameter.
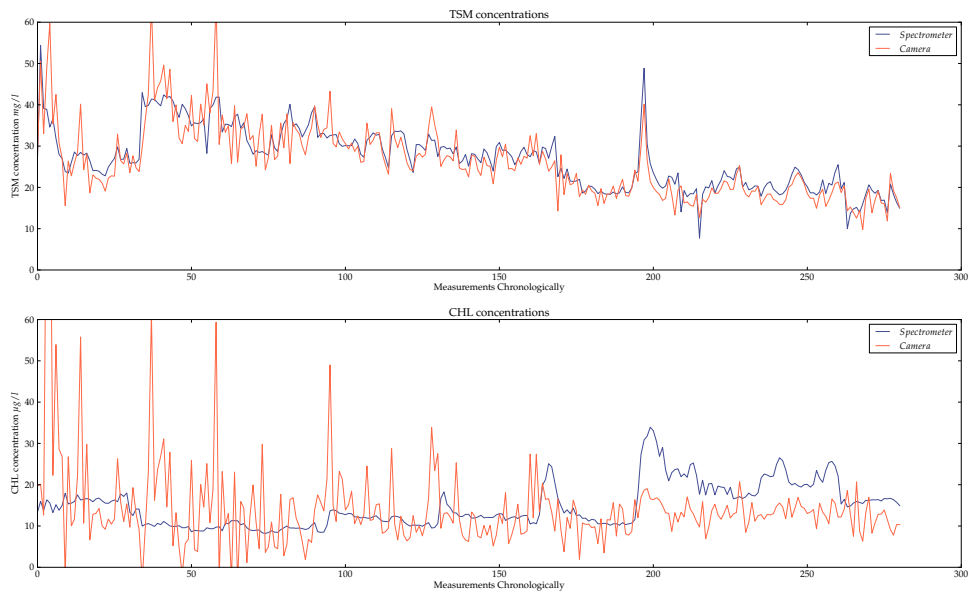

Figure 4.16: Overview of all of the concentrations measured with the spectrometer and the camera combined with the spectrometer.
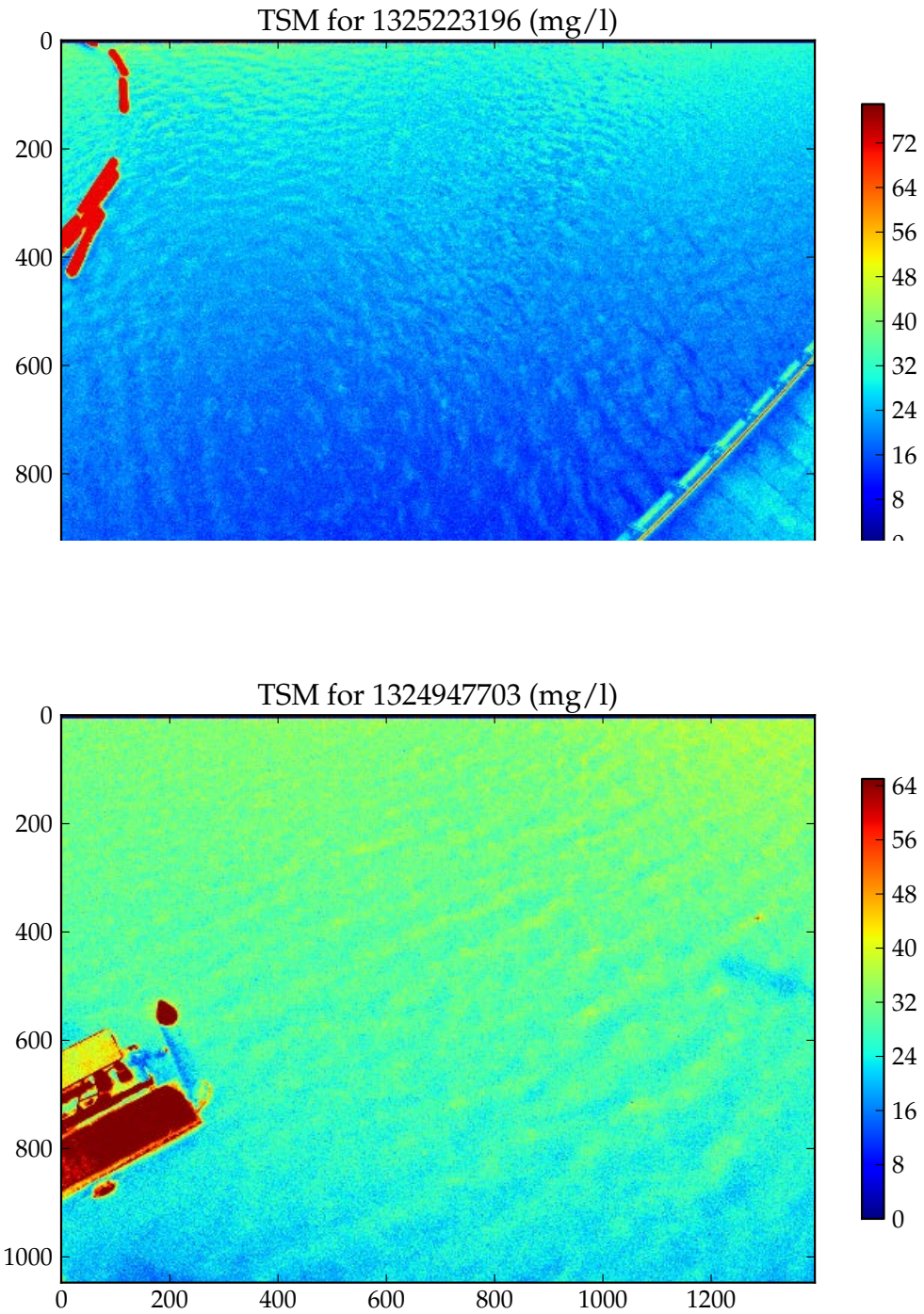
Figure 4.17: Output of two TSM maps that were created using the WICAM
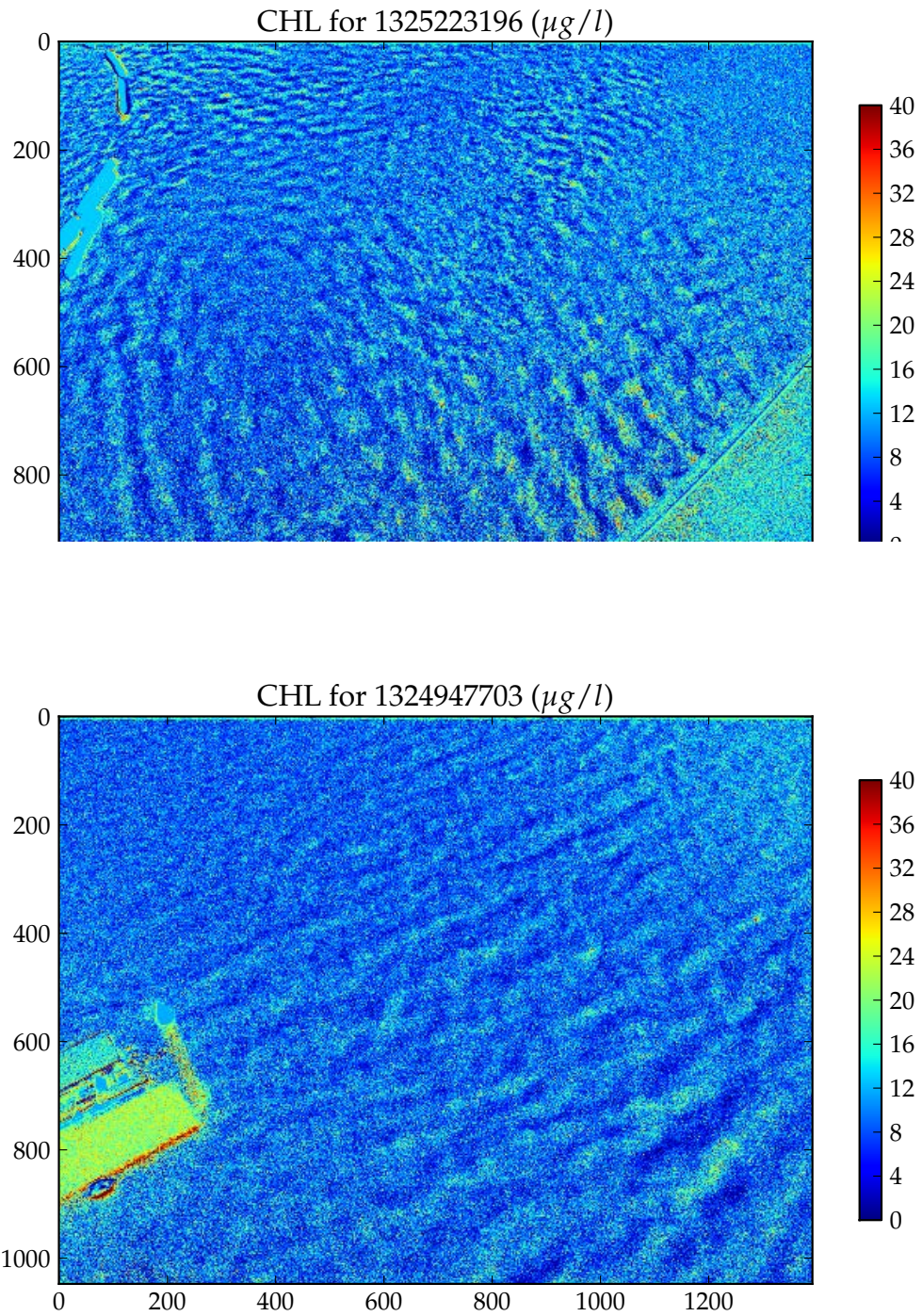
Figure 4.18: Output of two CHL maps that were created using the WICAM

The calculations were also performed using all of the camera pixels (see Figures 4.17 and 4.18) and the images that have been adjusted with the median filter (see Figure 4.19). In the TSM maps the above mentioned linear relationship TSM has with scattering is noticable in the gradient with rising concentrations of TSM the more one looks away from the sensor. The effect of waves on the concentrations is more visible in the CHL maps in Figure 4.18, causing high concentrations where the waves highest point in the one image band is at the same point as the waves lowest point in the next image band. Because of their distortions the CHL maps show that it is hard to classify concentrations as the image shows such a mixed end result. It is unclear if these results are accurate, or if this is caused by the gradient of light caused by the waves.

The raw data when processed shows the same noise and speckle that was identified in section 4.3 in the maps shown in Figures 4.18 and 4.17. To compare how the unfiltered images perform compared to the median filtered images, the three images were stacked next to each other. This shows interesting results. The filtered processed images show less noise and speckle but seem to exacerbate the effect the waves have on the concentration calculations. It is imperative to compare these values with in situ measurements of the water quality parameters to test the results that are produced in this research.

The results that have been produced using these algorithms and procedures to translate DNs to L_{water} values have not yet been verified by a ground truthing campaign. This is planned to be performed by the partners in the project. A few methods that would be good to take into account is research concerning in situ validation performed by Koponen et al. (2001, 2002) using Secchi disks and incorporating wind speed as a disturbing factor. A Secchi Disk is a cheap portable device that is very convenient for quick assessment of turbidity in the water (Holmes, 1970) and easy to relate to reflectance signals (Koponen et al., 2002). Wind speed is a parameter that gives insight into surface roughness, which is identified as quite a critical issue in estimating concentrations. The effect of wind speed is underlined by the results shown in Figure 4.19.

The dataset that was provided was large but is not really sufficient for deriving long term trends in the season nor a comparison between years. As the device is intended to be mounted for a longer period it would certainly be interesting to further investigate if trends can be detected in the dataset.

(c) Median 5x5 window
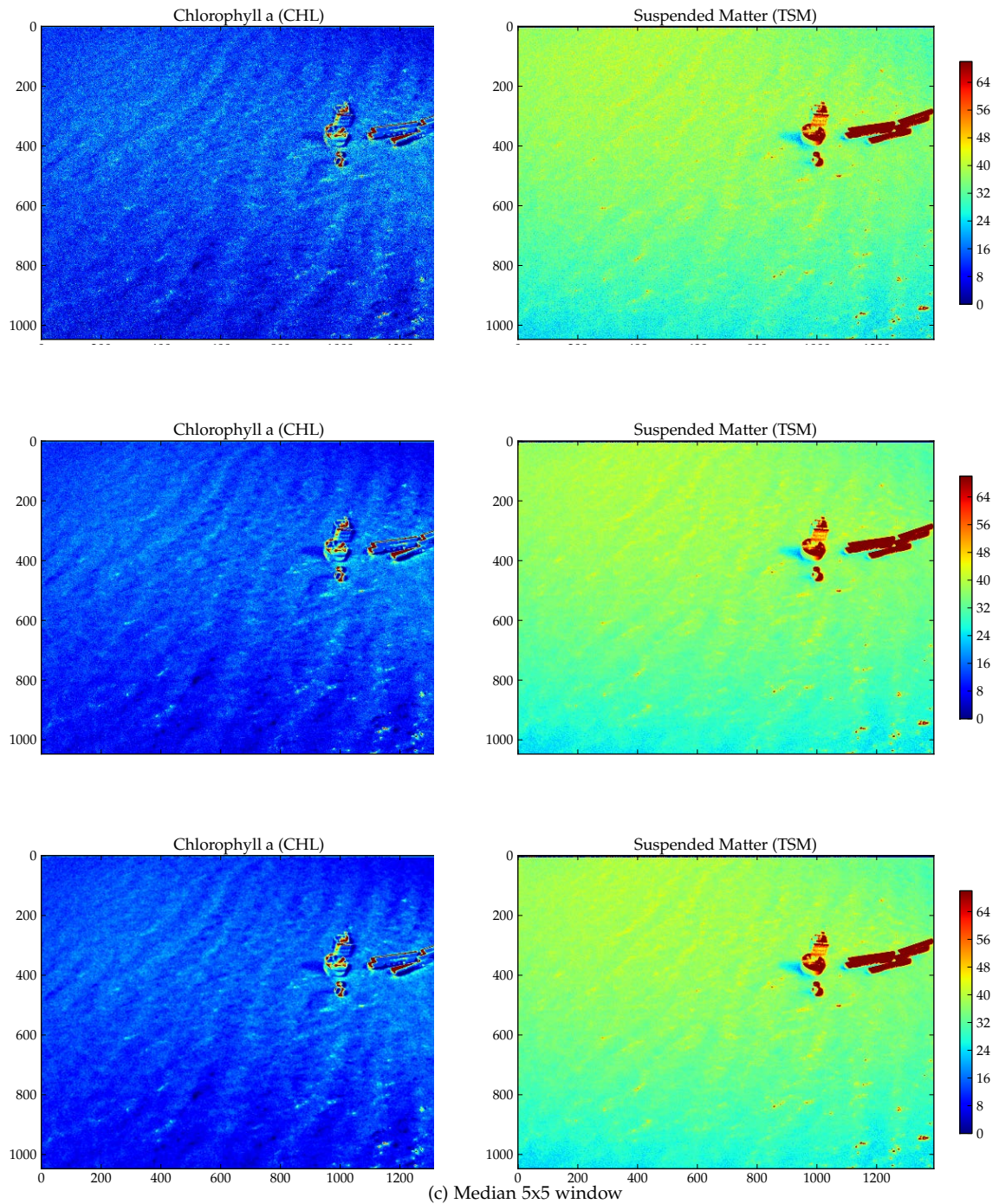
Figure 4.19: Difference between images with and without postprocessing Median filters of 3 and 5 – Measurement 1324870332.

Chapter 5

Conclusions & Recommendations

> Don't cry because it's over, smile because it happened
>
> ———————————————
>
> Dr. Seuss

5.1 Conclusions

The WICAM provides interesting results of spectral imagery and spectrometry measurements. These measurements have been correlated and analysed. The results hereof led to values that could be translated to water quality parameters. To answer the research question that was set up in this research sub-questions have been posed to help answer the main question. The answers to these sub-questions will be dealt with leading up to answering the main research question: *How can high resolution point data and spectral 2D images be integrated to provide one product for deriving water quality parameters?*

The correlation of these measurements is only as good as the measurements in themselves are. These measurements from the different instruments show good overall results. The spectrometry measurements are of high quality and are useful for deriving water quality products. The images taken with the camera are of varying quality. The water radiance measurement taken by the spectrometer, L_{water}, and the water photograph taken with the camera correlate highly. Among the six bands the correlation varies but it is very high, with a R^2 of 0.97 and higher where the spectrometer is measuring corresponding pixels in the image. The correlation between the other spectrometry measurements, the sky radiance L_{sky} and sky irradiance E_{sky} and the camera pixels is only a reflection of the total incoming light. The lower correlation of L_{sky} as opposed to E_{sky} is attributed to the narrow field of view of the L_{sky} measurement. Because of the high correlation between the images and the spectrometer, the camera pixels can be converted to the same L_{water} radiance values. The reflectance values per pixel can be calculated using the equations

41

used for the spectrometer and the spectrometry measurements L_{sky} and E_{sky}.

Variability is caused by a number of sources, some of which are simple, some of which are complex. The main source of variability in both simple and complex cases is light. The variable quality of the measurements that comes from the azimuthal solar angles is caused by the configuration of the WICAM. It is mounted with fixed angles and takes measurements at a fixed interval. Because of this only 40% of the measurements are usable. Even if the measurements comply with the solar angle filter, still a difference between measurements can be seen due to the sunlight direction. As mentioned the configuration of the WICAM also means a very limited FOV for the L_{sky} measurement. As a consequence the L_{sky} measurement can only be meaningful for a very specific part of the image, the part where the spectrometer measures L_{water}. The L_{sky} and E_{sky} spectra, are similar but not interchangeable. Therefore the sub-surface reflectance, $R(0-)$ which is calculated using all of the measurements, will not be completely reliable, which goes the same for the water quality products that are derived using this $R(0-)$.

Waves cause disturbance in the received signal of the camera. This is partly because the integration time of the spectrometer and the camera are different. But also because the camera itself does not take the images with different wavebands instantaneously, but there is some delay. Although the images are taken quickly, with a filter wheel rotating to speeds of 14,000 RPM, the effect of the wind on the water can still be seen in the images. The gradient of light and shade a wave causes is then at different locations for the different bands within the same sequence of images for every band. This is problematic because the calculations of concentrations depend on different wavebands.

Most of the issues that contribute to variability can quite easily be remedied. The solar azimuth angles by using a filter or by programming the device to only measure when the solar azimuth is correct. Besides the variability that is caused by light, the quality of the images is disturbed by quite some noise and speckle in the different image bands. This can result in faulty derivation of water quality parameters and ambiguous results. The images have therefore been smoothed with a median filter at different windows (3x3 and 5x5) to ameliorate the image quality. This yielded considerable improvement.

The integration of the WICAM as a whole, was twofold. One part was analyzing the different images in one sequence to compare the measurements that are next to each other. The second part was relating the digital number values of the camera to the water radiance L_{water}, calculating the sub-surface radiance $R(0-)$ and then calculating the concentrations of the water quality parameters CHL and TSM.

The first part, the different images in one sequence, clearly showed that images next to each other are highly related and as such can be used to create a integrated panoramic image of the whole bay area, instead of only the seperate images.

The second part, relating the images and the spectrometer to water quality parameters, showed that the WICAM can create a integrated product that shows water quality parameters such as CHL and TSM. For prediction for TSM it performs really well. The concentrations calculated with only the spectrometer and the camera and the spectrometer combined look very similar. For CHL this is not so good. This is mainly due to CHL being a parameter that is more susceptible to small differences as it is derived mainly from absorption features, whereas TSM is mainly derived from scattering features. Moreover TSM concentrations are known to "overshadow" CHL spectrally.

The integration of high resolution spectral point data and spectral 2D images to provide one product for deriving water quality parameters is non-trivial, but possible. The data that the WICAM produces needs preprocessing, filtering and conversion. Using the camera and the spectrometer combined, reflectance images can be produced that can be used to calculate concentrations of different parameters, such as Suspended Materials and Chlorophyll-a. These results are useful for comparison with in situ measurements. The concentration maps showed such results. It also showed that deriving water quality parameters still proves to be difficult, especially for deriving absorption features such as useful for Chlorophyll-a. The WICAM device is a good start in trying to accomplish this, but it also sets the stage for more research.

5.2 Recommendations

The questions that were set out to answer in this research have led to more questions. Following to discussion concerning the results in Chapter 4 it is imperative to write down recommendations for future research.

Ground Truthing

Ground truthing is essential for assessing the quality of spectrometry measurements and the derivative products it produces. However, ground truthing is lacking in this research. This is mainly due to a constraint in distance to the measuring device and the costs related to a journey for field work. The University of Singapore, Water Insight and Deltares are planning in situ measurements for ground truthing the WICAM. It would be very interesting to compare the in situ results with the resulting concentration calculations made with the WICAM.

Secchi Disk

In research carried out by Koponen et al. (2002) a number of methods to validate and compare water quality measurements with remote sensing images and spectroscopy were described. A number of parameters that can be assessed through the use of remote sensing are compared to in situ measurements of the same lake. One of the parameters which is easy to derive and easy to measure is the Secchi depth using the Secchi disk (Koponen et al., 2002). The Secchi disk is one of the most widely used instruments to assess

visibility which can serve as a proxy for turbidity (or TSM) in water (Holmes, 1970). It is very cheap and convenient to take to the field. This would be a good instrument to quickly and easily assess the quality of the derived parameters with the WICAM.

Wind Speed

As a large part of variability came from the surface roughness of the waves and the scattering of light it is adviced to take wind speed measurements at the measuring location. In research by Koponen et al. (2001) wind speed correction was performed. It is not exactly clear how this was done, nor is it discussed how much performance boost this yields. Nonetheless this seems an important step for improving the quality of the products derived with the WICAM.

Instrument Setup

The instruments setup of course is detrimental in defining the quality of the derived products. The way the calculations are defined in literature suggests that the high resolution of the measurements of the different spectrometers might not be necessary for the purpose it is serving, as most of the information comes from the higher filterbands and do not necessarily depend on a high resolution full spectrum. The recommended setup is using the filters that are used: 665, 703 nm and the filter at 776 nm. This is not configured in the setup yet, but the filter is necessary for the calculation of Chlorophyll-a with the use of the backscattering coefficient at 776 nm (see Equation 2.2). Once the WICAM is configured, tested and calibrated the use of the spectrometer measuring L_{water} becomes obsolete as the camera will measure more or less the same values.

Time Series

With the instrument configured in the way it is, it would be very interesting to look at the data on a yearly basis drawing conclusions on the whole time series. And subsequently look at different years if the instrument is still operational for a few years.

Appendix A

Correlation plots
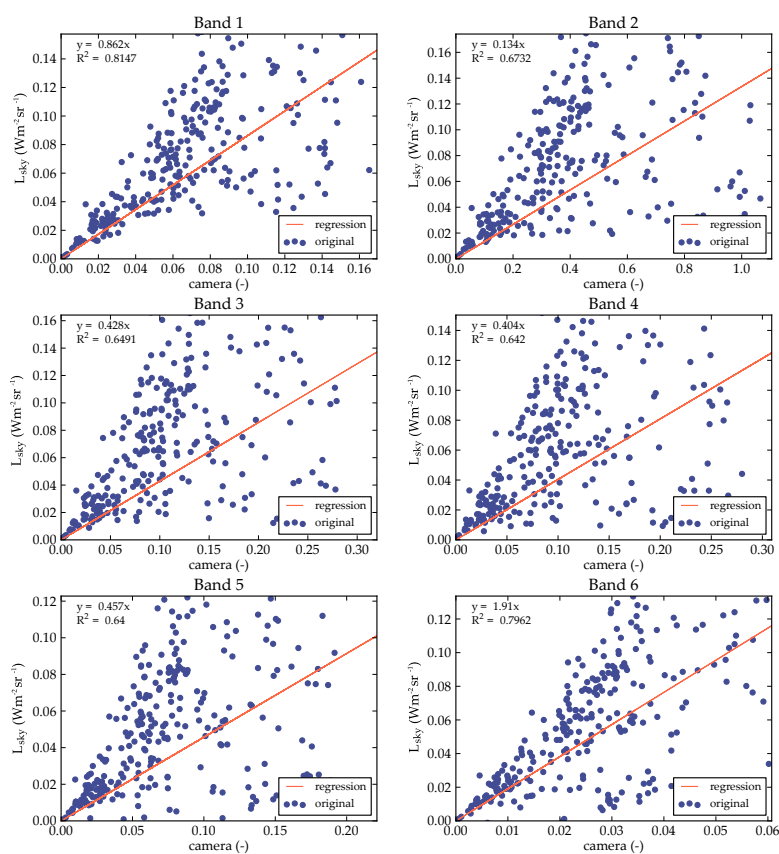
Figure A.1: Correlation between L_{sky} and the DNs of a subset of pixels.
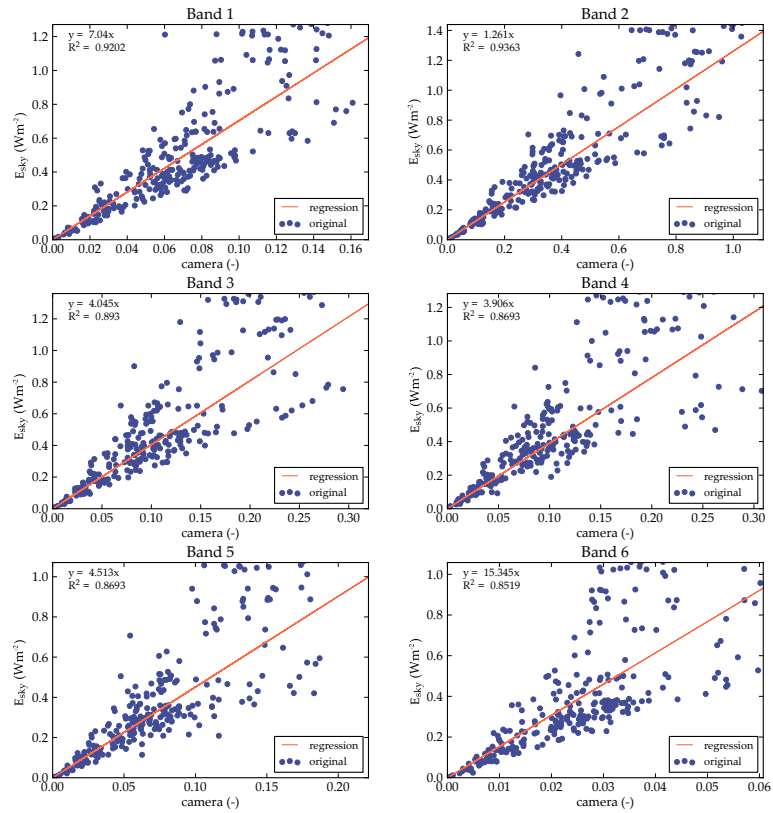
Figure A.2: Correlation between E_{sky} and the DNs of a subset of pixels.
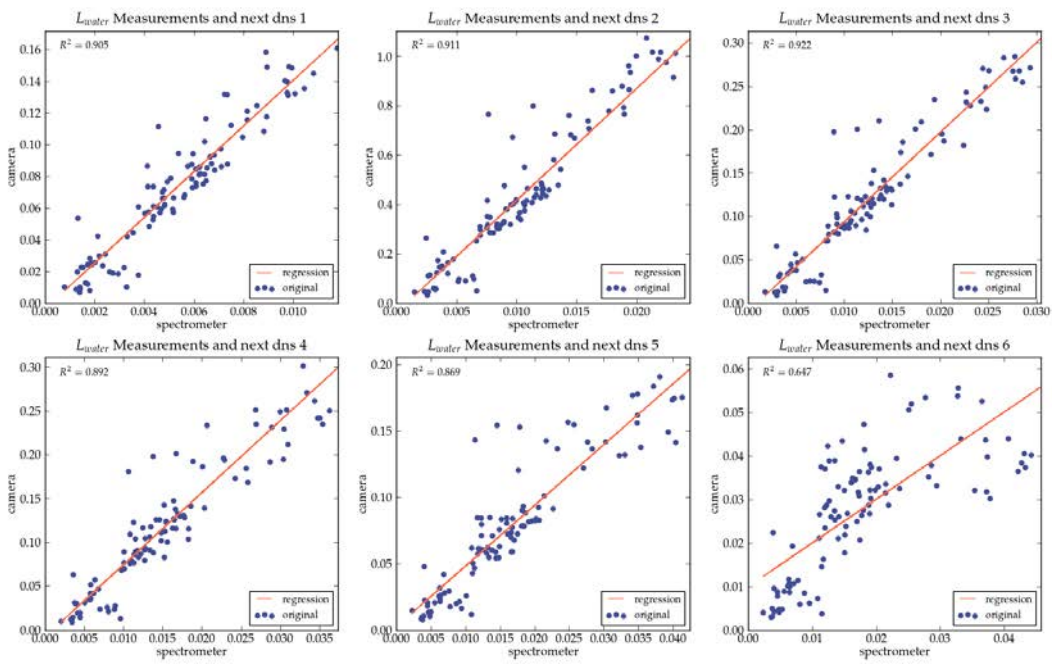
Figure A.3: Correlation between L_{water} and DNs of two measurements in one sequence that are next to each other.

References

Arrigo, K., Robinson, D., Worthen, D., Schieber, B., and Lizotte, M. (1998). Bio-optical properties of the southwestern ross sea. *Journal of Geophysical Research*, 103(C10):21683–21. 4

Bricaud, A., Bédhomme, A., and Morel, A. (1988). Optical properties of diverse phytoplanktonic species: Experimental results and theoretical interpretation. *Journal of Plankton Research*, 10(5):851. 4

Clavano, W. (2008). *Reflectance change due to surface roughness – With applications to ocean optics*. PhD thesis, Cornell University. 30

Cox, C. and Munk, W. (1954). Measurement of the roughness of the sea surface from photographs of the sun's glitter. *J. Opt. Soc. Am*, 44(11). 2

Curran, P. and Novo, E. (1988). The relationship between suspended sediment concentration and remotely sensed spectral radiance: a review. *Journal of Coastal Research*, pages 351–368. 32

Dekker, A. (1993). *Detection of Optical Water Quality Parameters for Entrophic Waters by High Resolution Remote Sensing*. PhD thesis. 5

Gitelson, A. and Merzlyak, M. (1996). Signature analysis of leaf reflectance spectra: algorithm development for remote sensing of chlorophyll. *Journal of plant physiology*, 148(3):494–500. 35

Gons, H. J. (1999). Optical Teledetection of Chlorophyll a in Turbid Inland Waters. *Environmental Science & Technology*, pages 1127–1132. 3, 5

Gons, H. J. (2005). Effect of a waveband shift on chlorophyll retrieval from MERIS imagery of inland and coastal waters. *Journal of Plankton Research*, 27(1):125–127. 6, 17, 27, 28

Govender, M., Chetty, K., and Bulcock, H. (2007). A review of hyperspectral remote sensing and its application in vegetation and water resource studies. *WaterSA*, 33(2):145–152. 1

Hakvoort, H., de Haan, J., Jordans, R., Vos, R., Peters, S., and Rijkeboer, M. (2002). Towards Airborne Remote Sensing of Water Quality in the Netherlands; validation and error analysis. *Survey Department, Rijkswaterstaat, Delft, The Netherlands*, pages 1–26. 1

Holmes, R. (1970). The secchi disk in turbid coastal waters. *Limnology and oceanography*, pages 688–694. 39, 44

Igawa, N., Koga, Y., Matsuzawa, T., and Nakamura, H. (2004). Models of sky radiance distribution and sky luminance distribution. *Solar Energy*, 77(2):137–157. 28

IOCCG (2000). Remote Sensing of Ocean Colour in Coastal , and Other Optically-Complex , Waters. Sathyendranath, S. (ed.), Reports of the International Ocean-Colour Coordinating Group. *IOCCG*, 3. iv, 1, 2, 4, 5, 24

Kallio, K. and Pulliainen, J. (2005). MERIS , MODIS and ETM + Channel Configurations in the Estimation of Lake Water Quality from Subsurface Reflectance Using Semi- analytical and Empirical Algorithms. *GeoPhysica*, 41:31–55. 11

Karpouzli, E. and Malthus, T. (2003). The empirical line method for the atmospheric correction of ikonos imagery. *International Journal of Remote Sensing*, 24(5):1143–1150. 18

Kiefer, D., Olson, R., and Wilson, W. (1979). Reflectance spectroscopy of marine phytoplankton. part 1. optical properties as related to age and growth rate. *Limnology and Oceanography*, pages 664–672. 4

Kirk, J. I. I. (1984). Dependence of relationship between inherent and apparent optical properties of water on solar altitude. *Limnology and Oceanography*, 29(2):350–356. 27

Kirk, J. T. O. (1994). *Light and Photosynthesis in Aquatic Ecosystems.*, volume 129. Cambridge University Press. 1, 2, 4, 9

Kirkpatrick, G., Millie, D., Moline, M., and Schofield, O. (2000). Optical discrimination of a phytoplankton species in natural mixed populations. *Limnology and Oceanography*, pages 467–471. 4

Koponen, S., Pulliainen, J., Kallio, K., and Hallikainen, M. (2002). Lake water quality classification with airborne hyperspectral spectrometer and simulated meris data. *Remote Sensing of Environment*, 79(1):51–59. 39, 43

Koponen, S., Pulliainen, J., Servomaa, H., Zhang, Y., Hallikainen, M., Kallio, K., Vepsäläinen, J., Pyhälahti, T., and Hannonen, T. (2001). Analysis on the feasibility of multi-source remote sensing observations for chl< i>-a</i> monitoring in finnish lakes. *Science of the total environment*, 268(1):95–106. 30, 39, 44

Laanen, M. (2007). *Yellow Matters*. Amsterdam Vrije Universiteit. 5

Mobley, C. D. (1999). Estimation of the remote-sensing reflectance from above-surface measurements. *Applied optics*, 38(36):7442–55. 2, 5, 6, 17

Morel, A. (1980). In-water and remote measurements of ocean color. *Boundary-Layer Meteorology*, 18(2):177–201. 4

OceanOptics. Jaz Data Sheet. *Technical Documents*, pages 1–52. 9, 10

Preisendorfer, R. (1961). *Application of radiative transfer theory to light measurements in the sea*. Institut géographique national. 5, 28

Preisendorfer, R. W. (1976). *Hydrologic Optics*. U.S. Dept. of Commerce, National Oceanic and Atmospheric Administration, Environmental Research Laboratories, Pacific Marine Environmental Laboratory,. 5, 28

Richards, J. A. and Jia, X. (2006). *Remote Sensing Digital Image Analysis: An Introduction*. Springer. 3

Ruddick, K., Nechad, B., Neukermans, G., Park, Y., Doxaran, D., Sirjacobs, D., and Beckers, J. (2008). Remote sensing of suspended particulate matter in turbid waters: State of the art and future perspectives. 35

Simis, S. (2006). *Blue-green catastrophe: remote sensing of mass viral lysis of cyanobacteria*. Dissertation, Vrije University Amsterdam. http://hdl. handle. net/1871/10641. 6

Tanaka, A., Kishino, M., Doerffer, R., Schiller, H., Oishi, T., and Kubota, T. (2004). Development of a neural network algorithm for retrieving concentrations of chlorophyll, suspended matter and yellow substance from radiance data of the ocean color and temperature scanner. *Journal of Oceanography*, 60(3):519–530. 35

Torgersen, C., Faux, R., McIntosh, B., Poage, N., and Norton, D. (2001). Airborne thermal remote sensing for water temperature assessment in rivers and streams. *Remote Sensing of Environment*, 76(3):386–398. 31

Vorosmarty, C. J., Green, P., Salisbury, J., and Lammers, R. (2000). Global Water Resources: Vulnerability from Climate Change and Population Growth. *Science*, 289(5477):284–288. 1

Weiss, B. (2006). Fast median and bilateral filtering. In *ACM Transactions on Graphics (TOG)*, volume 25, pages 519–526. ACM. 32